Study of Chemically Peculiar Stars: II. Asteroseismology of HD 23734, HD 68703, and HD 73345 using *K2-TESS* Space-based Photometry and High-resolution Spectroscopy

Santosh Joshi[1]★, Athul Dileep[1,2], Eugene Semenko[3], Mrinmoy Sarkar[1], Otto Trust[4], Peter De Cat[5], Patricia Lampens[5], Marc-Antoine Dupret[6], Surath C. Ghosh[1], David Mkrtichian[3], Sugyan Parida[7], Abhay Pratap Yadav[7], Pramod Kumar S.[8], Mathijs Vanrespaille[9], P. P. Goswami[10], Mohammad Riyas[11], Drisya Karinkuzhi[11],

[1]*Aryabhatta Research Institute of Observational Sciences, Manora Peak, Nainital- 263002, India*
[2]*Department of Applied Physics, M.J.P Rohilkhand University, Bareilly, Uttar Pradesh-243006, India*
[3]*National Astronomical Research Institute of Thailand (NARIT), Chiang Mai 50180, Thailand*
[4]*Department of Physics, Mbarara University of Science and Technology, P. O. Box 1410, Mbarara, Uganda*
[5]*Royal Observatory of Belgium (ROB), Ringlaan 3, B-1180 Brussels, Belgium*
[6]*Space Sciences, Technologies and Astrophysics Research (STAR) Institute, University of Liège, B-4000 Sart Tilman, Belgium*
[7]*Department of Physics and Astronomy, National Institute of Technology Rourkela, Sector 1, Rourkela - 769008, Odisha-India*
[8]*Indian Institute of Astrophysics, Koramangala, Bangalore-560034, India*
[9]*Institute of Astronomy, KU Leuven, Celestijnenlaan 200D, B-3001 Leuven, Belgium*
[10]*Dakshin Kamrup College, Gauhati University, Assam-781125-India*
[11]*Department of Physics, University of Calicut, Thenhipalam, Malappuram 673635, India*

Accepted DD Mmmm YYYY / Received DD Mmmm YYYY

ABSTRACT

We present space-based photometry, high-resolution spectroscopy, and seismic modeling of three stars, namely HD 23734, HD 68703, and HD 73345 that appeared as null results for pulsation in the Nainital-Cape survey project. We performed frequency analyses of the *K2* and *TESS* time-series photometric data of these three stars and found coexistence of rotation and pulsation. Spectrum synthesis was utilized to determine their basic physical parameters and chemical composition. The in-depth abundance analysis and fundamental parameters suggests that all the studied stars are chemically normal A-F type stars. The least squares deconvolution (LSD) profile analysis revealed line profile variations in all three stars, particularly more resolved in HD 68703. Evolutionary studies using a Hertzsprung–Russell (H-R) diagram indicate that HD 23734, HD 68703, and HD 73345 are located within the δ Scuti (δ Sct) instability strip close to the zero-age, middle-age, and terminal-age main sequence, respectively. Independent methods namely, period-luminosity relation, échelle diagrams, pulsation constant, Petersen diagram, and stellar pulsation models, were used to identify the modes of the detected frequencies. We identified five (n = 2, 4, 5, 6, and 7) radial modes in HD 23734, three (n = 1, 3, and 4) in HD 68703, and two (n = 1 and 5) in HD 73345. The seismic parameters, such as ages, luminosities, and effective temperatures from the best fit models were found to be comparable with the observed values. Through spectroscopic investigation we identified HD 23734 and HD 73345 as potential binaries, however, HD 68703 did not exhibit any radial velocity variation within the observational limit.

Key words: Asteroseismology – stars: chemically peculiar – stars: oscillations – stars: variables:, individual: HD 23734, HD 68703, HD 73345

1 INTRODUCTION

About 10% of the upper main-sequence (MS) stars (spectral types ~ early B to late F) exhibit distinct absorption features in terms of the intensity of spectral lines compared to normal stars of similar spectral types, ages, and populations. These are referred to as chemically peculiar (CP) stars showing overabundances of several orders of magnitude compared to the Sun for Silicon (Si), Chromium (Cr), Strontium (Sr), Europium (Eu), and other heavy elements (Ghazaryan et al. 2018). The CP stars are subdivided into four subgroups according to their effective temperature, the strength of their absorption lines and magnetic fields: the Am/Fm (CP1) stars, the Bp/Ap

★ E-mail: santosh@aries.res.in

(CP2) stars, the HgMn (CP3) stars, and the He-rich/poor (CP4) peculiar stars (Preston 1974; Paunzen et al. 2021). As candidate Am (A-metallic line) and Ap (A-peculiar) stars are the primary focus of this study, we briefly introduce the subclasses CP1 and CP2.

The Am/Fm stars are defined as non-magnetic stars characterized by either a deficiency of light elements such as C, N, O, Ca, Sc or an overabundance of Fe peak elements (e.g. Y, Ba) and/or rare earth elements (Conti 1970; Catanzaro et al. 2019). These A-type (Am) or early F-type (Fm) main-sequence stars share the same region as normal A-F type stars with effective temperatures ($T_{\rm eff}$) between 7000 and 9000 K. Most Am stars are slow rotators with projected rotational velocity ($\upsilon \sin i$) below 150 km s^{-1} and are generally found in binary systems with orbital periods ($P_{\rm orb}$) longer than 1.2 days (Iliev & Budaj 2008).

In contrast to Am stars, the Ap stars are magnetic and show anomalies of elements such as Si, Sr, Cr, Eu, and other rare-earth elements. In such stars, magnetic fields are generally dipolar with well-organized field lines and have a strength up to several tens of kilogauss (Bychkov et al. 2021) that varies periodically with time (Babcock 1947; Aurière et al. 2007). Although the exact origin of these fields is still unknown, it has been proposed that they are frozen-in during the formation of the star(Braithwaite & Spruit 2004; Aurière et al. 2007).

Chemical peculiarities are thought to have developed as a result of processes such as atomic diffusion or magnetic effects that either settle chemical elements into the quiet inner layers of slowly rotating stars or dredge them up to the surface layers (Michaud 1970; Richer et al. 2000). It is generally believed that the magnetic fields (in the case of Ap stars) and tidal synchronisation (in Am stars) are responsible for the slow rotation that minimizes turbulent mixing to operate the atomic diffusion efficiently (Abt & Snowden 1973; Shore & Adelman 1974; Ghazaryan & Alecian 2016). The Ap and Am stars are important in stellar astrophysics due to the presence of pulsations, inhomogeneities, slow rotation, and strong magnetic fields, which calls for careful asteroseismic modelling to understand their structure and evolution (Mikulášek et al. 2010; Krtička et al. 2013).

Previously, CP stars were not known to show pulsational variability (Breger 1970; Kurtz 1976). However, numerous Am and Ap stars are known to pulsate by now (Guzik et al. 2021; Holdsworth et al. 2024) thanks to the arrival of space missions such as *Kepler* and *TESS* (Bryson et al. 2010; Uytterhoeven et al. 2011; Lampens et al. 2013). Their huge amount of high-precision photometric data enabled the detection of low-amplitude pulsational signals in these stars, untraceable in data from ground-based telescopes. Multi-periodic δ Sct pulsations have been reported for a handful of Ap and Am stars (Smalley et al. 2017; Holdsworth et al. 2021; Dürfeldt-Pedros et al. 2024) covering the $T_{\rm eff}$-log g parameter space of the δ Sct instability strip in the Hertzsprung–Russell (H-R) diagram. They are crucial for testing stellar evolution models and understanding the mechanisms driving pulsations (Joshi & Joshi 2015; Paunzen 2024).

The δ Sct type variables are those falls at the intersection region between the main sequence and the classical instability strip on the Hertzsprung–Russel diagram with effective temperatures in the range $6300 < T_{\rm eff} < 9000$ K, $0.6 < \log(L/L_{\odot}) < 2.0$, and masses (M) between 1.5 and 2.5 $M_{\odot}$. Their evolutionary stages range from pre-main sequence to just evolved off the main sequence (about 2 mag above the ZAMS). They exhibit radial and/or non-radial pulsations, with low-order gravity (g) and/or pressure (p) modes with pulsation periods ranging from $\sim$ 15 min to $\sim$ 8 h (e.g; Rodríguez & Breger 2001; Buzasi et al. 2005; Guzik 2021). The pulsation in δ Sct is driven by the κ-mechanism operating in the He II partial ionisation zone (Baker & Kippenhahn 1962; Steindl et al. 2022) and the turbulent pressure acting in the hydrogen ionization zone (Antoci et al. 2014). The δ Sct-type pulsators are an interesting class of objects owing to their existence in the transition region between stars having a convective ($M < 2\,M_{\odot}$) or a radiative ($M > 2\,M_{\odot}$) envelope making them an intriguing class of pulsating variables and help to probe the stellar envelope. Detailing the mechanisms of excitation and mode selection in δ Sct stars represents a significant unresolved problem in stellar pulsations, since their masses fall within a region where convective zones are forming in the outer layer of the star.

In the late 1990s, the "Nainital-Cape (NC) Survey" was commenced between astronomers from India and South Africa. This investigation resulted in the discovery of the first far northern roAp star HD 12098 from ARIES Nainital (Martinez et al. 2001; Kurtz et al. 2024). Using ground-based time-resolved photometric and spectroscopic observations anomalous pulsations were reported in half a dozen CP stars by Joshi et al. (2003, 2006, 2009, 2010, 2012, 2016, 2017). In the new era of space photometry, Joshi et al. (2022) discovered the first heartbeat CP star HD 73619 with the absence of tidally induced pulsations. Leveraging the extensive light curves provided by the *TESS* space mission, an asteroseismic analysis of HD 118660 was conducted recently by Sarkar et al. (2024). Based on spectroscopic observations from HESP (India) and HERMES spectrographs under the Indo-Belgium collaborative project, NLTE analysis of a group of hot CP stars was carried out by Trust et al. (2020, 2021, 2023). A recent study by Dileep et al. (2024) revisited the classification of four sample stars in the NC survey using TESS photometry and compiled a table with variability classes for all stars observed by TESS in the survey based on Balona (2022). We have also initiated the search for pulsating CP stars in open clusters using ground-based facilities to circumvent the poor spatial resolution of the TESS observations (Dileep et al. 2025). Thus, with the participation of the astronomers from many nations this bilateral effort emerged as a global collaboration in the area of asteroseismology.

The NC Survey includes 381 objects under investigation, none of which were observed by the *Kepler* space mission. However, *K2* data is available for eight NC Survey targets. Of these, five were classified as rotational variables by Joshi et al. (2022), while the remaining three (HD 23734, HD 68703, and HD 73345) turned out to be pulsating variables. This paper focuses on these three stars on combining the space-based photometric observations from *K2* and *TESS* with multi-epoch ground-based spectroscopy to provide a comprehensive analysis.

The manuscript is structured as follows. In Sec. 2 we discuss the photometric observations from *TESS* and *K2* missions and their frequency analysis along with an overview of the spectroscopic observations and adopted data reduction techniques. The detailed spectroscopic analysis to determine fundamental parameters and individual abundances along with the evolutionary status of the stars are given in Sec. 3. In Sec. 4 we determine the seismic stellar parameters through identification of the radial modes from the observed freqeuncies. Finally, in Sec. 5, we discuss the results for individual stars, followed by our conclusions and future prospects of the present study in Sec. 6.

2 OBSERVATIONS AND DATA REDUCTION

2.1 *K2* and *TESS* Photometry

The *K2* (Kepler two-wheel) mission initiated observations on February 4, 2014, and concluded on September 26, 2018. The observation covered 105° × 105° in the Cousins R band along the ecliptic was

Table 1. The observational information on the targets observed by *K2* and *TESS* space missions from the MAST archive. The available campaigns/sectors for each star and their cadences are listed.

Star	Mission	Campaigns/ Sectors	Cadence (s)
HD 23734	*K2*	4	1800
	TESS	42, 43, 44	120
	TESS	70, 71	200
HD 68703	*K2*	5, 18	1800
	TESS	44, 45, 46	120
	TESS	71, 72	200
HD 73345	*K2*	5, 18	1800
	TESS	44, 45, 46	120
	TESS	72	200

split into 19 campaigns, each with a duration of 80 days (Howell et al. 2014). The *K2* mission offers two data types: short-cadence (1 min) and long-cadence (30 min), with an angular resolution of 4 arcsecs per pixel, thereby minimizing the likelihood of contamination from neighbouring stars. The accuracy of *K2* photometry is inferior to that of Kepler photometry owing to inaccurate pointing, causing a drift within the field of view.

The Transiting Exoplanet Survey Satellite (*TESS*) (Ricker et al. 2015) launched in 2018 is an all sky photometric survey mission that uses the Cousins I band to cover 90% of the sky, except for a narrow band along the ecliptic. During the primary phase of *TESS*, observations in 26 sectors within a $24^\circ \times 96^\circ$ field of view have been done. Each hemisphere was divided into 13 sectors and monitored for one year, with each sector observed for 27.4 days. The angular resolution per pixel for *TESS* is 21 arcsec, leading to a diminished spatial resolution that results in blending and contamination from neighbouring stars. Overlap exists between sectors at the extreme northern and southern ecliptic latitudes, leading to the observation of specific stars in multiple sectors. The *TESS* primary mission data products comprise short cadence observations every 2 min for designated stars and full-frame images (FFIs) acquired every 30 min for all stars within the field of view. The extended *TESS* mission began on July 4, 2020, featuring a cadence of 20 sec for brief observations and 10 min or 200 sec for extended observations, facilitating a thorough re-examination of all sectors for an equivalent duration.

The details of the data available for different sectors in *TESS* and campaigns in *K2* are provided in Table 1. The data products were retrieved using the Python module LIGHTKURVE (Lightkurve Collaboration et al. 2018) downloaded from the Barbara A. Mikulski Archive for Space Telescopes[1] (MAST). We utilized the Pre-search Data Conditioning Simple Aperture Photometry (PDCSAP) flux in both instances, as it is detrended using the Co-trending Basis Vectors (CBVs), eliminating most of the telescope's systematic trends. Before performing the frequency analysis, we eliminated the outliers, transformed the flux into relative milli-magnitude scale(mmag), and subsequently normalized the light curves to zero by subtracting the mean light variation.

2.1.1 *Frequency Analyses*

The frequency analyses of the light curves was conducted using the `Period04` program (Lenz & Breger 2005). The periodogram was computed over a frequency range from zero to $\nu_{Nq} = \frac{1}{2\Delta t}$, where Δt represents the time sampling and ν_{Nq} denotes the Nyquist frequency, defined as the maximum frequency resolvable in a frequency spectrum. For the long cadence (Δt = 29.43 min) and short cadence (Δt = 120 sec) data, the values of ν_{Nq} are ~24.27 d^{-1} and ~360 d^{-1}, respectively. We combined successive sectors for each star, avoiding longer gaps in the time series to minimize aliasing. The resultant frequency spectrum was iteratively prewhitened by fitting the frequencies, amplitudes, and phases to a sinusoidal function corresponding to the frequency of the highest peak. The fitted sinusoids were subsequently subtracted from the light curve iteratively until the signal-to-noise ratio (SNR) of the residual peaks were less than 5.4 (Baran et al. 2015). The uncertainties in the frequencies and amplitudes were calculated using the methodology proposed by Montgomery & O'Donoghue (1999). Two adjacent frequencies with a separation less than 2.5 times the Rayleigh resolution (1/Δ T) were considered as unresolved (Loumos & Deeming 1978). Figs. A1-A6 shows the light curves (left panels) and periodograms (right panels) of the stars in the individual *K2* campaigns and *TESS* sectors. We discovered amplitude modulation in several detected frequencies across the individual sectors of all the stars, a finding that warrants further investigation. A comparison of frequency spectra of HD 23734, HD 68703, and HD 73345, from *K2* and *TESS* are displayed in Figs. 1, 2, and 3, respectively. It is evident that the short cadence *TESS* data allowed us to detect more frequencies compared to *K2*. Tables 2, 3 & 4 lists the frequencies extracted from the combined time series data and the corresponding pulsation constants (Q-values) for the detected radial modes (Breger 1990).

2.2 Spectroscopy

For this study, we used the data acquired from dedicated observing facilities and archives. A set of high-resolution spectra for each star was collected using the Hanle Echelle Spectrograph (HESP; Chanumolu et al. (2015); Sriram et al. (2018)) mounted on the 2.01-m Himalayan Chandra Telescope (HCT) of the Indian Astronomical Observatory (IAO) and Medium-Resolution Échelle Spectrograph (MRES) of the 2.4 m Thai National Telescope (TNT). One high-resolution spectrum of HD 23734 and four high-resolution spectra of HD 68703 were collected with the High-Efficiency and High-Resolution Mercator Echelle Spectrograph (HERMES; de Cuyper et al. (2007); Raskin et al. (2011)) of the 1.2-m Mercator telescope installed in La Palma, Spain. The raw spectra were reduced using the dedicated pipelines available for the HESP and HERMES. MRES data was processed to result in one-dimensional wavelength-calibrated spectra using the up-to-date version of a Python-based pipeline written by one of the authors (ES)[2].

An observation of HD 68703, conducted under project *ID 110.248M.001* using the intermediate resolution XSHOOTER spectrograph (Vernet et al. 2011) at the 8.2-m Very Large Telescope (VLT), was retrieved through the Science Portal of the European Southern Observatory (ESO) [3]. The medium- and low-resolution spectra of HD 23734 and HD 73345 were also extracted from the archive of the Large Sky Area Multi-Object Fiber Spectroscopic Telescope (LAMOST; Cui et al. 2012, Zhao et al. 2012)[4] from Data Release 10 (DR10).

[1] https://archive.stsci.edu/

[2] Python-based Yet Another Pipeline (PyYAP) source code: https://github.com/ich-heisse-eugene/PyYAP

[3] https://archive.eso.org/scienceportal/home

[4] LAMOST DR10. https://www.lamost.org/dr10/v2.0/search

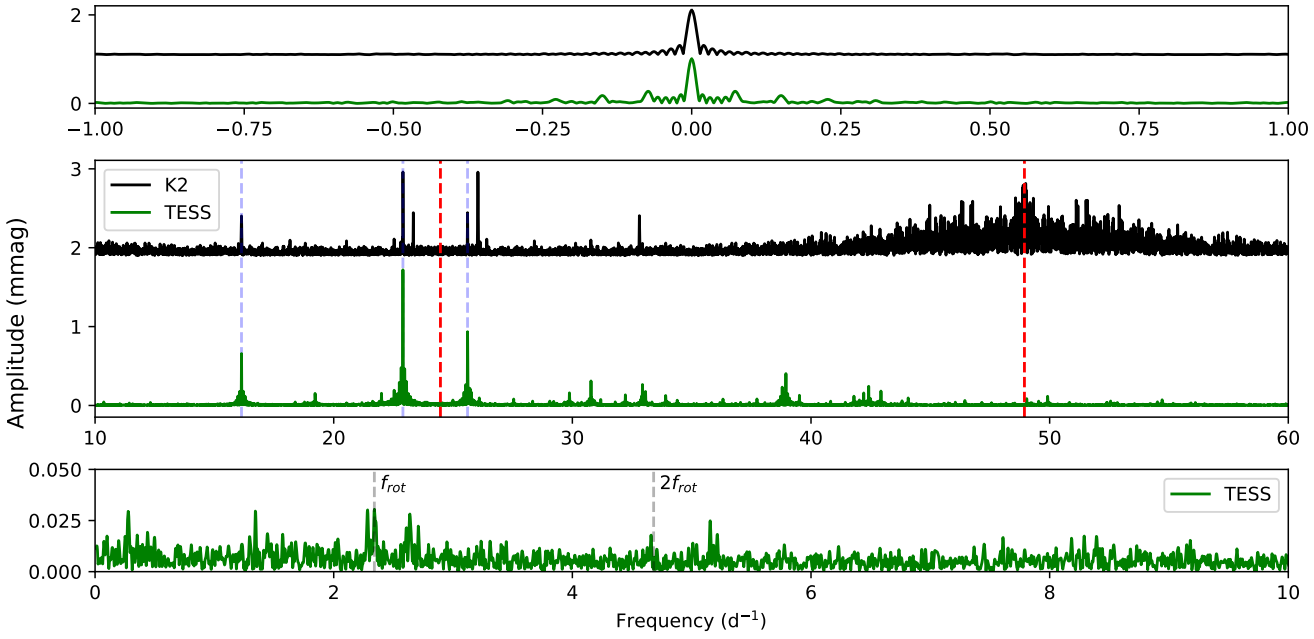

Figure 1. The top panel shows the window function for campaign 4 data of *K2* (black) and *TESS* (green) combined data (sectors 42, 43 and 44) sets for the star HD 23734. The lower panel compares the frequency spectra obtained for the light curves of *K2* and *TESS*. The frequency spectra from *K2* are added by 1.8 mmag for visual clarity. The red vertical dashed lines indicate the integer multiples of the Nyquist frequency of *K2*. The blue dashed lines indicate the common frequencies in *K2* and *TESS*. The bottom panel shows the low-frequency range of HD 23734.

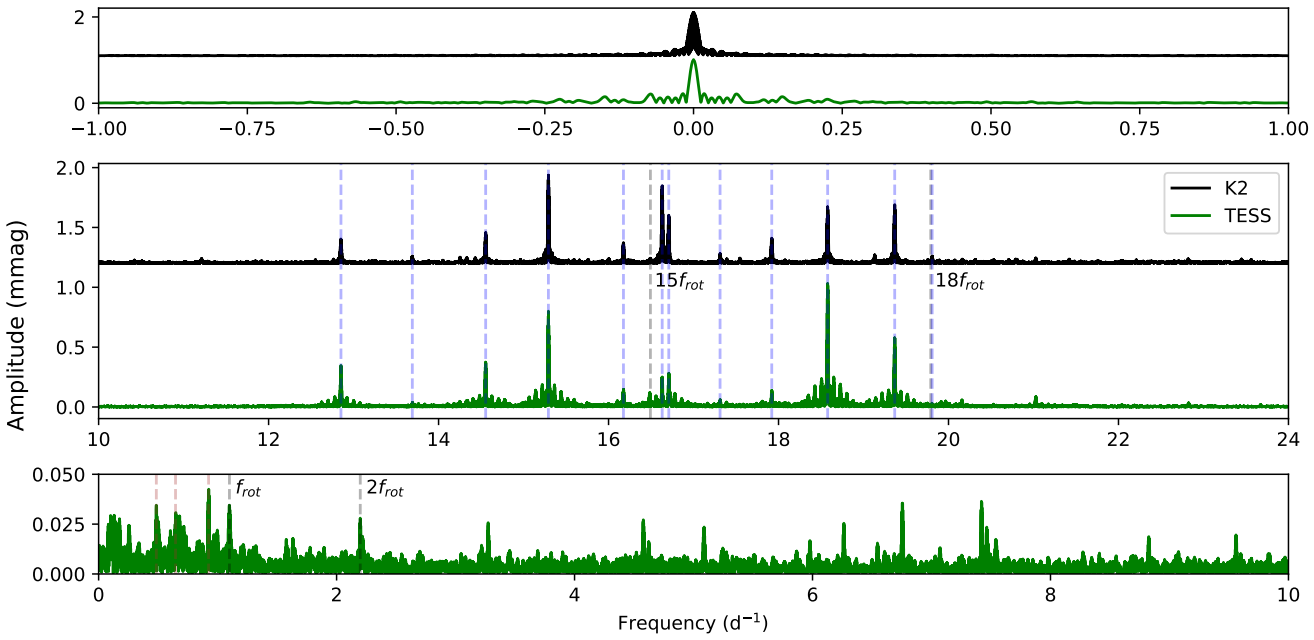

Figure 2. Idem as Fig. 1 but for HD 68703 with *TESS* (sectors 44, 45, and 46) and *K2* (campaigns 5 and 18). Here all the frequencies are within the Nyquist limit of both *K2* and *TESS*. The bottom panel indicates the low-frequency range of HD 68703, the possible rotational frequency and its harmonics are marked with dashed black lines in the middle and bottom panels. The brown vertical dashed lines correspond to the unidentified low frequencies, which are significant.

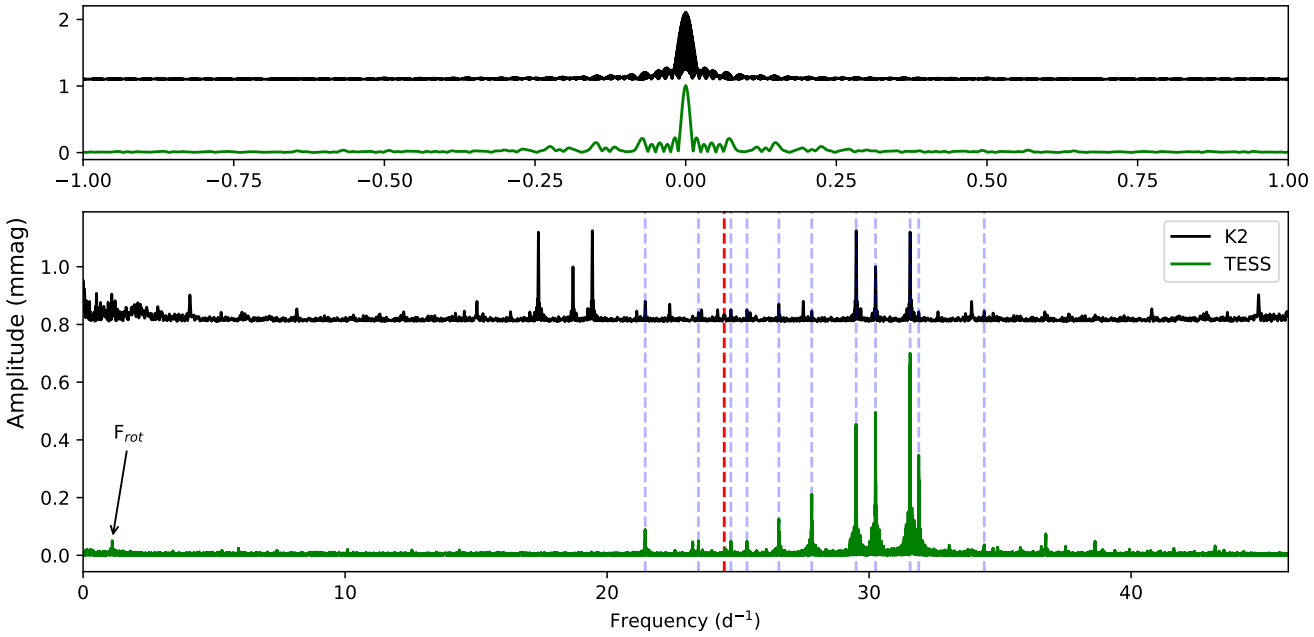

Figure 3. Same as Fig. 1 but for HD 73345 with *TESS* (sectors 44, 45 and 46) and *K2* (campaigns 5 and 18). We do not plot lower frequencies separately here. We point to the rotational peak with an arrow.

The wavelength scale of medium- and high-resolution spectra was calibrated using a Th-Ar reference source. The wavelengths were corrected for the barycentric motion. All spectra were normalised to the continuum level using the task CONTINUUM of the Image Reduction and Analysis Facility[5] (IRAF). The signal-to-noise ratio (SNR) of the spectra was evaluated at the wavelength of 550 nm. The details of the spectroscopic observations are summarised in Table 5. We also tabulate the observed radial velocity (RV) and projected rotational velocity ($\upsilon \sin i$) for each spectra.

3 STELLAR FUNDAMENTAL PARAMETERS AND EVOLUTIONARY STATUS

From measuring the spectra, one can directly estimate parameters such as effective temperature ($T_{\rm eff}$), surface gravity ($\log g$), and projected rotational velocity ($\upsilon \sin i$). The stellar chemical composition can be evaluated through individual atomic abundances (for example $\log N_{\rm el}/N_{\rm tot}$) or metallicity ([M/H]). Metal lines in the spectra of CP stars are crucial for peculiarity classification, offering valuable information on the specific types of peculiar stars being examined. At least three parameters, $T_{\rm eff}$, $\log g$, and [M/H], can be found indirectly using the existing calibrations of different photometric indices. We used photometrically derived temperature and surface gravity as the initial values of corresponding parameters in spectroscopic analysis.

3.1 Interstellar extinction

Photometric calibrations of stellar parameters are sensitive to the interstellar reddening. To ensure the proper accounting for this effect, first, we looked into the 3D Dustmap Bayestar (Green 2018; Green et al. 2019) models. Given the *Gaia* parallaxes (Gaia Collaboration 2018) and stellar Galactic coordinates from SIMBAD database[6] (Wenger et al. 2000), these maps showed zero reddening for all three stars. However, a study of the interstellar extinction maps presented by Lallement et al. (2022) and Vergely et al. (2022) revealed non-zero values of cumulative absorption A_{550} at wavelength λ = 550 nm, which is nearly equivalent to more common parameter A_V, in all three cases. The strongest absorption is expected for HD 23734: A_{550} = 0.086 mag. The values of A_{550} for HD 68703 and HD 73345 are 0.025 and 0.039 mag, respectively.

More accurately, reddening can be evaluated spectroscopically from interstellar absorption lines of sodium doublets (Na D1 and D2 lines). In an available set of spectra, the interstellar features around Na D1 and D2 have been securely detected only for the star HD 23734. To convert the measured equivalent widths W_λ(D1) = 100 mÅ and W_λ(D2) = 85 mÅ to the colour excess E_{B-V} we used an empirical correlation established by Poznanski et al. (2012). After multiplication E_{B-V} by 3.11, this gives us the total absorption A_V = 0.06–0.10 mag, in a good agreement with A_{550}, found for HD 23734 earlier. A probe for interstellar lines in spectra of HD 68703 and HD 73345 revealed no measurable features. Thus, to calculate the luminosity of the programme stars, we adopted the values of A_{550} and listed them in Table 6.

3.2 Fundamental parameters and chemical composition

3.2.1 Photometry based evaluation

We, first of all, used the Geneva (Golay 1980; Rufener & Nicolet 1988), $uvby\beta$ (Strömgren 1963, 1966; Crawford & Mander 1966;

[5] https://iraf-community.github.io/

[6] https://simbad.u-strasbg.fr/simbad/

Table 2. The frequencies, corresponding amplitude and signal-to-noise ratio (SNR) for HD 23734 were obtained through the combined analysis of the three consecutive sectors namely 42, 43, and 44 of *TESS* time-series data. Similarly, the frequency solution for *K2* data of single campaign 4, are also listed. The pulsation constant (Q) for the identified radial modes and combination of different frequencies are also tabulated. Here, only the short cadence of *TESS* data was used to avoid aliasing and find the actual frequencies beyond the Nyquist (Nyq) limit from *K2*.

		TESS			
	f (d^{-1})	Amp (±0.003 mmag)	SNR	Q-value (days)	Comb. Freqs.
fr_1	22.90016±0.00001	1.727	309.8	0.0267	F2
fr_2	25.60789±0.00003	0.936	175.4	-	5F6-5F5
fr_3	16.13569±0.00004	0.662	126.6	-	-
fr_4	38.94782±0.00006	0.446	75.7	0.0157	F5
fr_5	30.78033±0.00008	0.308	58.4	-	2F4-15F_{rot}
fr_6	38.79358±0.00009	0.286	49.0	-	2F2-3F_{rot}
fr_7	32.93878±0.00009	0.265	42.1	0.0185	F4
fr_8	42.4168±0.0001	0.246	44.3	-	-
fr_9	22.5310±0.0001	0.221	40.8	-	F5-7F_{rot}
fr_{10}	25.7210±0.0001	0.208	39.4	-	11F_{rot}
fr_{11}	42.9315±0.0001	0.185	31.1	-	3F2-11F_{rot}
fr_{12}	33.0666±0.0002	0.160	24.3	-	-
fr_{13}	29.8766±0.0002	0.165	29.6	-	10F4-6F7
fr_{14}	42.2087±0.0002	0.164	29.5	-	16F4-11F6
fr_{15}	22.0017±0.0002	0.160	28.8	-	-
fr_{16}	19.2192±0.0002	0.156	30.8	-	18F_{rot}-F2
fr_{17}	32.2210±0.0002	0.141	22.2	-	-
fr_{18}	33.9091±0.0002	0.131	24.4	-	-
fr_{19}	39.5157±0.0002	0.124	20.6	-	-
fr_{20}	41.7995±0.0002	0.128	23.1	-	20F4-14F6
fr_{21}	49.9145±0.0002	0.117	18.6	0.0122	F7
fr_{22}	26.0984±0.0002	0.101	18.5	-	2F4-17F_{rot}
fr_{23}	44.0720±0.0003	0.096	16.3	0.0139	F6
fr_{24}	22.4092±0.0003	0.091	16.6	-	2F2-10F_{rot}
fr_{25}	49.0387±0.0003	0.087	12.3	-	-
fr_{26}	37.7358±0.0003	0.086	15.7	-	14F7-15F6
fr_{27}	36.3113±0.0003	0.082	12.6	-	-
fr_{28}	27.5403±0.0003	0.080	15.0	-	-
fr_{29}	42.0281±0.0003	0.078	14.0	-	9F5-7F6
fr_{30}	31.1892±0.0003	0.074	13.6	-	F7-8F_{rot}
fr_{31}	54.7124±0.0003	0.074	12.5	-	3F4-F6
fr_{32}	34.3933±0.0004	0.070	11.6	-	-
fr_{33}	24.9947±0.0004	0.064	11.2	-	-
fr_{34}	46.4479±0.0004	0.063	9.9	-	-
fr_{35}	40.8229±0.0004	0.056	10.3	-	-
fr_{36}	43.8136±0.0004	0.056	9.1	-	18F4-11F7
fr_{37}	52.5559±0.0005	0.054	9.0	-	9F7-9F6
fr_{38}	29.2187±0.0004	0.056	11.9	-	5F7-5F6
fr_{39}	29.0548±0.0005	0.053	11.1	-	-
fr_{40}	49.5389±0.0005	0.053	8.1	-	-
fr_{41}	28.3355±0.0005	0.051	10.9	-	-
fr_{42}	21.6257±0.0005	0.051	9.7	-	9F4-12F2
fr_{43}	18.7759±0.0005	0.046	9.2	-	3F2-F7
fr_{44}	33.3351±0.0005	0.045	7.0	-	-
fr_{45}	54.5173±0.0006	0.045	7.2	-	2F5-10F_{rot}
fr_{46}	18.3873±0.0006	0.044	8.8	-	4F5-6F2
fr_{47}	30.3839±0.0006	0.045	8.3	-	-
fr_{48}	29.6660±0.0006	0.044	8.5	-	-
fr_{49}	31.7962±0.0006	0.043	7.0	-	11F5-9F6
fr_{50}	46.0459±0.0006	0.041	6.9	-	2F6-18F_{rot}
fr_{51}	10.3633±0.0006	0.041	9.7	-	12F2-6F6
fr_{52}	37.0475±0.0006	0.040	7.6	-	F6-3F_{rot}
fr_{53}	41.4372±0.0006	0.039	7.1	-	9F2-5F4
fr_{54}	36.1861±0.0006	0.039	5.8	-	
fr_{55}	56.1051±0.0006	0.038	6.5	-	8F6-9F4
fr_{56}	50.8394±0.0006	0.039	7.2	-	-
fr_{57}	37.4168±0.0006	0.038	6.9	-	16F_{rot}
fr_{58}	21.6767±0.0006	0.039	7.2	-	9F4-12F2
fr_{59}	47.1537±0.0007	0.037	6.4	-	2F4-8F_{rot}
fr_{60}	12.3188±0.0007	0.037	7.1	-	3F7-6F2
fr_{61}	18.9915±0.0007	0.037	7.4	-	5F7-7F4
fr_{62}	52.8368±0.0007	0.036	5.6	-	2F2+3F_{rot}
fr_{63}	2.3406±0.0007	0.034	4.8	-	F_{rot}
fr_{64}	4.660±0.001	0.018	3.5	-	2F_{rot}
		K2			
f_{K1}	22.9001±0.0007	1.1±0.1	22.0	-	-
2Nyq-f_{K2}	25.608±0.001	0.5±0.1	10.7	-	-
f_{K3}	16.136±0.002	0.5±0.1	9.1	-	-

Hauck & Mermilliod 1998), and 2MASS (Cutri et al. 2003) photometry to derive stellar fundamental parameters. Combining the colour indices from various photometric systems aimed to reduce discrepancies caused by potential binarity significantly influencing the system's total flux. Photometrically derived parameters were later tuned using the spectra fitting technique.

In our sample, Geneva photometric indices are available only for HD 68703 and HD 73345 (Paunzen 2022). By applying the calibrations published by Kunzli et al. (1997) to the indices $B2-V1$, d and $m2$, we have found $T_{\rm eff}$=7180 K, log g=4.02 for HD 68703, and $T_{\rm eff}$=7980 K, log g=4.50 for HD 73345, respectively. As for metallicity [M/H], calibration gives values 0.2–0.35 for both stars. One can note an abnormally higher value of the surface gravity for HD 73345, which we interpret later.

The photometric indices of the $uvby\beta$ system can be found for all three stars in a paper by Paunzen (2015). To analyse them, we use the calibrations developed by Moon & Dworetsky (1985) and improved by Napiwotzki et al. (1993). This gives us information about $T_{\rm eff}$, log g, and [M/H] of the studied stars.

As for the photometry in the 2MASS system, we only use it to estimate stellar effective temperatures through the relations published by Casagrande et al. (2021). Multiple values of $T_{\rm eff}$ corresponding to different indices have been averaged and given in Table 6 together with the rest of the parameters evaluated for two other photometric systems. The uncertainties in $T_{\rm eff}$, log g, and [M/H] were determined from the scattering of the individual data.

3.2.2 *Spectroscopic approach*

Unlike photometry, spectroscopic analysis provides a more accurate way of measuring multiple parameters from one observation. We utilised a spectrum fitting technique to quantify the programme stars' fundamental parameters and chemical composition.

We use the IDL implementation of the Spectroscopy Made Easy (SME; Valenti & Piskunov 1996; Piskunov & Valenti 2017) to fit the model spectra to the medium and high-resolution observational data. Our analysis is based on the grid of Atlas9 models built-in into the package. The line lists were acquired from the Vienna Atomic Line Database (VALD; Piskunov et al. 1995; Kupka et al. 2000; Ryabchikova et al. 2015) for the values of $T_{\rm eff}$ and log g found earlier from photometry.

Using the photometric $T_{\rm eff}$, log g, and [M/H] as the input parameters, we further refined $T_{\rm eff}$ and [M/H] by fitting the hydrogen lines in LAMOST and XSHOOTER spectra. We prefer this kind of data to high-resolution observations because the Balmer lines in echelle spectra of early-type stars usually span a significant fraction of orders, making accurate continuum normalisation impossible. The effective temperature and metallicity measured in this way are shown in Table 7. In the next step, while fitting high-resolution spectra from HESP and HERMES, we searched for log g, $\xi_{\rm mic}$, and individual abundances. To this, the effective temperature was fixed, the hydrogen lines were masked, and the metallicity was set to zero. Table 7 lists the results of fitting excepting abundances.

3.2.3 *Stellar rotation*

Rotational broadening of spectral lines was evaluated using the Least-Squares Deconvolution (LSD) method (Donati & Brown 1997). The mask necessary for deconvolution was compiled from the linelists retrieved from VALD according to the derived basic parameters for each star. We fitted LSD profiles with a rotationally broadened line

Table 3. Idem as Table 2 but for HD 68703. Here we combined consecutive *TESS* sectors 44, 45, and 46, along with *K2* light curves from campaigns 5 and 18 combined. No frequencies beyond the *K2* Nyquist limit were detected in this case.

	TESS						*K2*		
	f (d^{-1})	Amp (±0.002 mmag)	SNR	Q-value (d)	Comb. Freqs.		f (d^{-1})	Amp (±0.006 mmag)	SNR
f_{T1}	18.57798±0.00001	1.032	246.9	0.0155	F4	f_{K4}	18.577989±0.000006	0.0189	69.9
f_{T2}	15.29221±0.00002	0.783	179.3	0.018	F3	f_{K1}	15.292443±0.000004	0.737	119.6
f_{T3}	19.36695±0.00002	0.641	145.0	-	-	f_{K3}	19.366866±0.000006	0.481	63.1
f_{T4}	14.55409±0.00003	0.365	106.9	-	-	f_{K6}	14.55414±0.00001	0.268	48.7
f_{T5}	12.85130±0.00003	0.358	127.5	-	F1+3F_{rot}	f_{K8}	12.85119±0.00001	0.207	48.3
f_{T6}	16.70863±0.00004	0.326	83.2	-	-	f_{K5}	16.709372±0.000007	0.385	50.9
f_{T7}	16.63107±0.00004	0.328	82.9	-		f_{K2}	16.632078±0.000004	0.645	84.5
f_{T8}	17.92033±0.00007	0.188	47.8	-	-	f_{K7}	17.92044±0.00001	0.213	35.4
f_{T9}	16.17536±0.00009	0.139	33.0	-	F1+6F_{rot}	f_{K9}	16.17520±0.00002	0.180	22.4
f_{T10}	21.0273±0.0002	0.077	17.1	-	7F3-9F1	-	-	-	-
f_{T11}	16.4889±0.0002	0.072	17.9	-	15F_{rot}	-	-	-	-
f_{T12}	17.3132±0.0002	0.065	18.5	-	-	f_{K13}	17.31204±0.00004	0.078	10.6
f_{T13}	19.9153±0.0002	0.050	11.4	-	3F1-8F_{rot}	-	-	-	-
f_{T14}	20.1599±0.0002	0.052	12.6	-	-	-	-	-	-
f_{T15}	13.6909±0.0003	0.046	16.8	-	10F4-18F1	f_{K18}	13.69112±0.00005	0.058	11.4
f_{T16}	22.8251±0.0003	0.044	12.7	-	4F1-14F_{rot}	-	-	-	-
f_{T17}	0.9242±0.0003	0.042	7.0	-	-	-	-	-	-
f_{T18}	0.6464±0.0003	0.039	6.3	-	18F_{rot}-2F1	-	-	-	-
f_{T19}	19.9664±0.0003	0.041	9.4	-	-	-	-	-	-
f_{T20}	0.4850±0.0003	0.042	6.7	-	-	-	-	-	-
f_{T21}	6.7560±0.0003	0.040	11.8	-	-	-	-	-	-
f_{T22}	2.1989±0.0003	0.039	9.4	-	2F_{rot}	-	-	-	-
f_{T23}	7.4194±0.0003	0.038	12.2	-	4F4-7F1	-	-	-	-
f_{T24}	17.3882±0.0003	0.036	10.0	-	2F3-12F_{rot}	-	-	-	-
f_{T25}	16.1046±0.0003	0.039	9.3	-	-	-	-	-	-
f_{T26}	1.0995±0.0004	0.033	5.9	-	F_{rot}	-	-	-	-
f_{T27}	17.8126±0.0004	0.032	8.6	-	-	-	-	-	-
f_{T28}	21.4722±0.0004	0.030	7.1	-	-	-	-	-	-
f_{T29}	19.8069±0.0004	0.031	7.3	-	18F_{rot}	f_{K17}	19.80777±0.00005	0.061	8.4
f_{T30}	19.6983±0.0004	0.030	7.3	-	F4+F_{rot}, F3+4F_{rot}	-	-	-	-
f_{T31}	3.2738±0.0005	0.027	7.6	-	3F_{rot}	-	-	-	-
f_{T32}	4.5788±0.0005	0.027	6.8	-	-	-	-	-	-
f_{T33}	20.5333±0.0005	0.027	6.0	-	F1+10F_{rot}	-	-	-	-
f_{T34}	17.5449±0.0005	0.027	7.2	-	10F4-11F3	-	-	-	-
f_{T35}	23.6716±0.0005	0.023	6.6	-	-	-	-	-	-
f_{T36}	9.5603±0.0007	0.018	6.5	0.0310	F1	-	-	-	-
-	-	-	-	-	-	f_{K15}	16.58560±0.00004	0.076	9.8
-	-	-	-	-	-	f_{K16}	19.13116±0.00004	0.063	8.9

profile to determine $\upsilon \sin i$ of the stars (Fig. 4). The results of fitting are tabulated in Table 5. From spectrum fitting using SME, we derived the following values of $\upsilon \sin i$ for the studied stars: HD 23734 — 133 km s^{-1}, HD 68703 — 66 km s^{-1}, HD 73345 — 85 km s^{-1}.

The averaged profiles of stars HD 23734 and HD 73345 exhibit minimal line profile variations, attributable to their pulsation and comparatively higher rotational broadening. However, HD 68703 shows a visible change in the line profiles, due to their relatively small rotational broadening, which can be interpreted as the effect of pulsation. Thus HD 68703 is an ideal candidate for further studying the line profile variations (LPV).

3.2.4 Atmospheric Abundances

Individual chemical abundances were determined by subdividing HESP spectra into segments, covering absorption lines and suitably normalised continuum. The spectrum synthesis was used to assess all significant elements in each segment. The atmospheric abundances are presented for the studied stars in Table 8 and the same is depicted in Fig. 5 with respect to the solar composition taken from Asplund et al. (2021); Magg et al. (2022). Our analysis shows that all the target stars are chemically normal, with the observed abundances close to the solar values. However, a small excess or deficiency of some elements can not be entirely ruled out given the errors of the abundance determination exceeding 0.7 dex or more. The latter cases in Table 8 are marked with the colon sign.

3.2.5 Stellar multiplicity

We measured the radial velocity from the available spectra, which are listed in Table. 5. One can notice that HD 23734 and HD 73345 show significant RV variations greater than expected for pulsations. Unfortunately, due to the lack of well sampled spectroscopic observations, we could not draw any firm conclusion on the period of variability or binarity, hence more follow-up spectroscopic observations are essential to confirm the binarity nature of HD 23734 and HD 73345. However, HD 68703, exhibited RV variations within the limit of ~3 km/s, hence considered as a single star based on the avaiable radial velocity measurements.

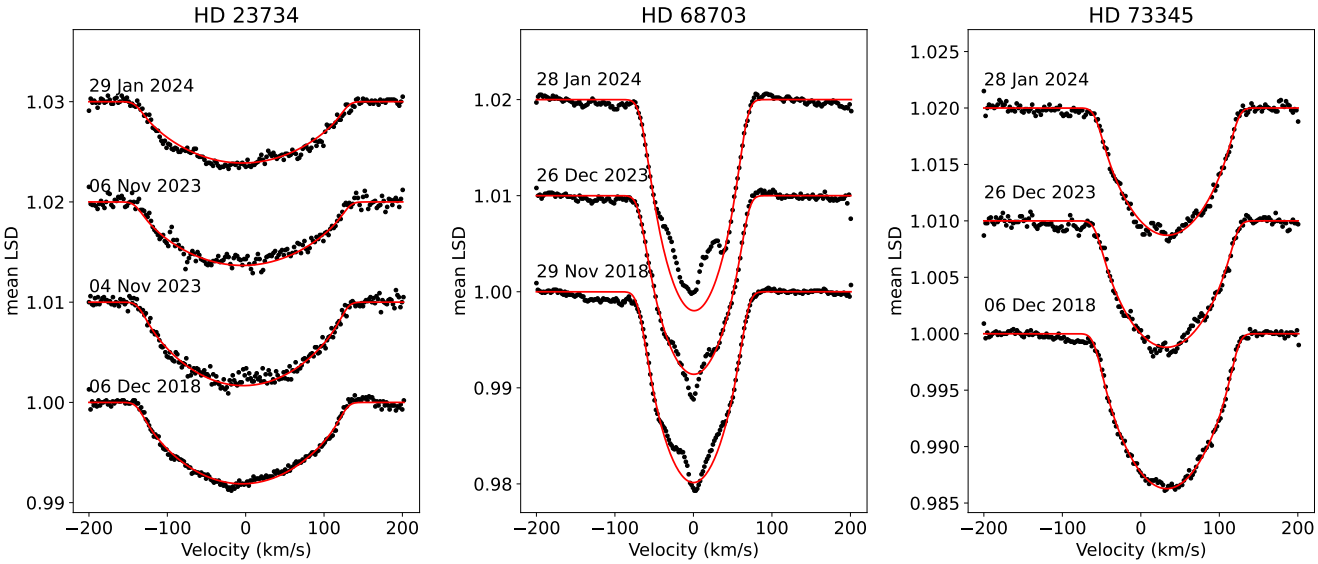

Figure 4. *Left Panel:* The mean LSD profiles of HD 23734 for the spectra taken on four different nights. The broadening of the profile clearly indicates large rotational velocity evident from Table 5. *Middle panel:* LSD profiles of HD 68703 obtained for three nights where one can notice the periodic line profile variations. *Right panel:* LSD profiles for HD 73345 extracted on three different nights. In all the panels, the red fitted lines represent the rotational broadening profile.

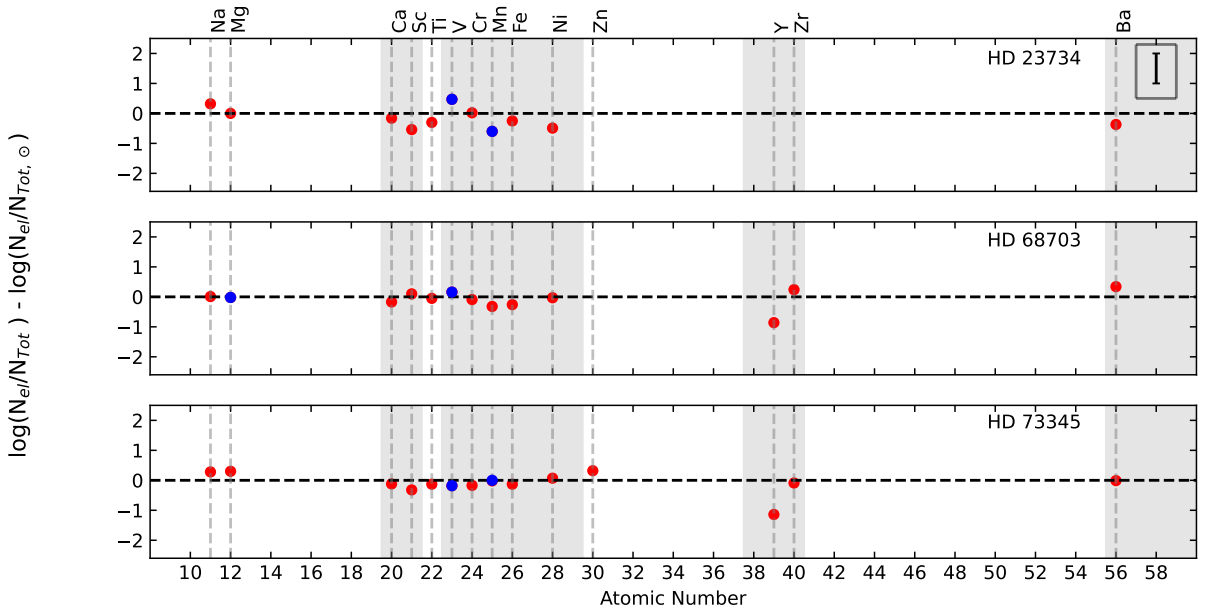

Figure 5. The relative abundance of the elements calculated from the high-resolution spectroscopic data. The horizontal black dashed line represents solar abundances from Asplund et al. (2009) while the vertical grey dashed lines imply the one-to-one mapping of the names of the elements and corresponding atomic numbers. The blue dots represent the underestimated abundances. The box at the upper right corner of the plot gives the typical size of error bars on the data points. The shaded regions enclose the important elements for chemical peculiarity classification.

Table 4. Same as Table 2 but for HD 73345. Here, we combined consecutive *TESS* sectors 44, 45, and 46, along with *K2* light curves from campaign 5 and 18.

	TESS					*K2*			
	f (d^{-1})	Amp (±0.003 mmag)	SNR	Q-value	Comb. Freqs		f	Amp (±0.006 mmag)	SNR
f_{T1}	31.56558±0.00003	0.694	154.0	0.0148	F5	2Nyq-f_{K1}	31.56564±0.00001	0.285	107.2
f_2	30.24686±0.00005	0.473	108.4	-	-	2Nyq-f_{K3}	30.24688±0.00001	0.203	77.0
f_{T3}	29.50692±0.00005	0.458	112.1	-	-	2Nyq-f_{K2}	29.50709±0.00001	0.331	130.0
f_{T4}	31.89596±0.00006	0.372	80.8	-	-	2Nyq-f_{K7}	31.89610±0.00004	0.064	22.6
f_{T5}	27.8107±0.0001	0.191	42.0	-	-	2Nyq-f_{K8}	27.80985±0.00006	0.048	19.7
f_{T6}	26.5554±0.0002	0.123	27.2	-	-	2Nyq-f_{K6}	26.55562±0.00004	0.066	24.8
f_{T7}	21.4556±0.0003	0.089	22.8	-	-	f_{K5}	21.45574±0.00003	0.081	32.6
f_{T8}	36.7432±0.0003	0.081	20.3	-	-	-	-	-	-
f_{T9}	1.1119±0.0004	0.055	8.1	-	F_{rot}	-	-	-	-
f_{T10}	25.3400±0.0004	0.051	11.7	-	-	2Nyq-f_{K13}	25.34047±0.00008	0.032	10.5
f_{T11}	23.4880±0.0005	0.047	11.3	-	-	f_{K9}	23.48595±0.00008	0.035	12.2
f_{T12}	24.7246±0.0005	0.047	10.8	-	-	2Nyq-f_{K10}	24.72477±0.00008	0.035	11.8
f_{T13}	38.6261±0.0005	0.046	9.8	-	3F1-4F_{rot}	-	-	-	-
f_{T14}	23.2674±0.0005	0.045	10.8	-	F1+8F_{rot}	-	-	-	-
f_{T15}	34.3951±0.0007	0.034	6.4	-	F1+18F_{rot}	2Nyq-f_{K12}	34.39525±0.00008	0.034	10.7
f_{T16}	33.0620±0.0007	0.034	7.0	-	3F1-9F_{rot}	-	-	-	-
f_{T17}	43.2062±0.0007	0.033	7.6	-	2F1+13F_{rot}	-	-	-	-
f_{T18}	37.5039±0.0008	0.030	7.2	-	3F1-5F_{rot}	-	-	-	-
f_{T19}	36.5739±0.0008	0.029	7.4	-	F1+20F_{rot}	-	-	-	-
f_{T20}	35.7724±0.0009	0.027	5.8	-	-	-	-	-	-
f_{T21}	10.095±0.001	0.022	5.6	-	-	-	-	-	-
f_{T22}	14.360±0.001	0.022	5.4	0.0325	F1	f_{K19}	14.2104±0.0001	0.022	7.0
-	-	-	-	-	-	f_{K4}	15.03217±0.00001	0.210	67.9
-	-	-	-	-	-	f_{K11}	19.25318±0.00008	0.035	14.1
-	-	-	-	-	-	f_{K15}	18.8381±0.0001	0.025	9.3
-	-	-	-	-	-	f_{K16}	8.1570±0.0001	0.023	6.0

3.3 Evolutionary Status

To determine the evolutionary phase of the sample stars, we locate the studied stars in the H-R diagram. To this, we used the luminosities derived from *Gaia* parallaxes and $T_{\rm eff}$ from high-resolution spectra. The absolute magnitudes ($M_{\rm V}$) were estimated using *Gaia* parallaxes (Gaia Collaboration et al. 2016) using the standard relation (Cox 2000), with the trigonometric parallax (π) measured in arcsec. For the calculation of the stellar luminosity ($\log(L/L_{\odot})$), we adopted the solar bolometric magnitude as $M_{bol,\odot}$ = 4.73 mag (Torres 2010). The bolometric correction (BC) was estimated from empirical relations from Torres (2010). The values of absolute magnitude ($M_{\rm V}$) and $\log(L/L_{\odot})$ along with their errors are listed in Table 6.

The position of HD 23734, HD 68703, and HD 73345 in the H-R diagram are shown in Fig. 6. The evolutionary tracks for different stellar masses ranging from 1.6 to 2.0 $M_{\odot}$ and ages of range 0.1-1.4 Gyrs calculated with stellar evolution code CLÉS (Code Liégeois d'Evolution Stellaire (Scuflaire et al. 2008a), are also depicted. The theoretical γ Dor (Dupret et al. 2004) and observational δ Sct (Murphy et al. 2019) instability strips are overplotted. The location of HD 23734 near the zero-age main sequence (ZAMS: age ~ 0.8 Gyr) suggests this star has started core hydrogen burning. HD 68703 is situated near the terminal age main sequence (TAMS: age ~ 1.2 Gyr), where the hydrogen in the core is nearly exhausted. HD 73345 is situated between the ZAMS and TAMS (age ~ 1.0 Gyr), suggesting that it is actively burning hydrogen in its core. On inspecting the frequency spectra and the position of the studied stars within the instability strips, one can conclude that HD 23734, HD 68703 and HD 73345 belong to the δ Sct pulsating variables.

4 MODE IDENTIFICATION AND SEISMIC MODELLING

Mode identification in δ Sct stars places a considerable challenge owing to the complexity of their frequency spectra. The detected frequency corresponding to highest amplitude is most likely to be of low-order radial mode, since the amplitudes of high angular degree modes ($\ell \geq 4$) tend to cancel each other out due to the cancellation effect (Aerts et al. 2010). To identify the radial modes from the detected frequencies, we can apply independent techniques and compare their results. In the following subsections, we discuss the methods used for the mode identification.

4.1 Period-Luminosity Relation

Pulsating stars have been known to follow well-defined relations between their period and luminosity, such as in δ Sct, Cepheids, RR Lyrae and other pulsating variables. Various authors have established the Period-Luminosity (P-L) relation for δ Sct stars (Ziaali et al. 2019; Poro et al. 2021) and improved them over time. Recently, Barac et al. (2022) revisited the P-L relation for the fundamental mode of δ Sct stars and put forward an improved empirical relation,

$$M_V = (-3.01 \pm 0.07)\log(P/\text{days}) - (1.40 \pm 0.07) \quad (1)$$

where P is the period of the fundamental radial mode expressed in days (d). In Fig. 7, we depicted the graphical representation of Eq. 1. The scatter points are the position of the stars with M_V estimated from the *Gaia* DR3 parallax, and the extinction (A_V) of the individual stars is considered from Na line (Joshi et al. 2017). The fundamental frequencies (f_1) for HD 68703 and HD 73345 are detected from the short cadence data of the TESS lightcurve at $9.56d^{-1}$ and $14.36d^{-1}$, respectively. However, the fundamental frequency for HD 23734 is not directly detected from TESS or K2 light curves.

Table 5. The overview of the spectroscopic observations. Here, we show the averaged observed parameters on the nights with time-series observations.

Object	Telescope	Diameter (m)	Spectrograph	Date (UT)	BJD (2400000+)	Resolution ($\lambda/\Delta\lambda$)	Integration Time (sec)	SNR (@550 nm)	RV (km/s)	$\upsilon \sin i$ ($\pm$ 1 km s^{-1})
HD 23734	LAMOST	4.0	LRS	16 Jan 2018	58135.0181	1800	1800	140	-1.3 ± 3.1	-
				06 Jan 2019	58490.0631	1800	1800	227	-5.8 ± 1.8	-
	HCT	2.01	HESP	06 Dec 2018	58459.3276	30000	1200	137	-4.8 ± 0.4	133
				06 Nov 2023	60255.1806	30000	1200	40	-4.6 ± 0.9	134
				29 Jan 2024	60339.2102	30000	900	75	-4.4 ± 0.7	135
	Mercator	1.20	HERMES	04 Nov 2023	60252.5708	85000	200	60	-3.4 ± 0.5	132
	TNT	2.4	MRES	13 Feb 2025	60720.0171	18500	900	170	4.0 ± 1.8	138
HD 68703	VLT UT3	8.2	XSHOOTER	22 Dec 2022	59935.8470	11333	10	366	0.0 ± 4.5	-
	LAMOST	4.0	MRS	27 Dec 2017	58115.2472	7500	600	164	-	-
				28 Nov 2018	58451.3479	7500	1200	21	-	-
				19 Dec 2018	58472.2812	7500	1200	21	-	-
				27 Dec 2018	58480.3013	7500	1200	41	-	-
				11 Feb 2019	58526.1180	7500	1200	11	-	-
				04 Jan 2021	59219.2638	7500	1200	79	-	-
	HCT	2.01	HESP	29 Nov 2018	58452.4225	30000	1200	103	-0.3 ± 0.2	69
				26 Dec 2023	60305.2285	30000	900	222	0.2 ± 0.2	68
				28 Jan 2024	60338.4145	30000	900	162	0.6 ± 0.2	65
				07 Mar 2025	60742.1224	30000	900	146	0.8 ± 0.2	68
				07 Mar 2025	60742.3348	30000	900	168	0.7 ± 0.2	68
	TNT	2.4	MRES	18 Dec 2024	60663.2273	18500	410	200	2.3 ± 0.2	69
				19 Dec 2024	60664.4384	18500	389	222	1.0 ± 0.2	68
				13 Feb 2025	60720.0672	18500	420	200	2.6 ± 1.1	67
	TBL	2.0	NARVAL	12 Jan 2007	54113.6120	65000	600	266	1.46 ± 0.05	68
				17 Jan 2007	54118.6024	65000	600	296	1.45 ± 0.07	68
	Mercator	1.20	HERMES	15 Mar 2025	60750.5739	85000	300	148	0.9 ± 0.2	68
				15 Mar 2025	60750.5819	85000	300	173	1.3 ± 0.2	68
				16 Mar 2025	60751.4649	85000	300	151	1.0 ± 0.2	68
				16 Mar 2025	60751.5914	85000	300	134	0.9 ± 0.2	67
HD 73345	LAMOST	4.0	LRS	04 Jan 2016	57392.2045	1800	1800	312	24.9 ± 2.1	-
				27 Jan 2016	57415.1631	1800	2100	140	28.4 ± 3.3	-
				24 Feb 2016	57443.1606	1800	1800	255	29.8 ± 2.2	-
	HCT	2.01	HESP	06 Dec 2018	58459.3733	30000	1200	79	32.5 ± 0.2	90
				26 Dec 2023	60305.2426	30000	900	55	32.4 ± 0.4	89
				28 Jan 2024	60338.4302	30000	900	63	33.0 ± 0.3	89
	TNT	2.4	MRES	13 Feb 2025	60720.0945	18500	900	160	37.1 ± 1.2	90

Table 6. The basic physical parameters of the target stars taken from the SIMBAD database (Columns 2–4). The parameters listed in the remaining columns are estimated from the photometric calibrations, were the mean photometric parameters for each stars are marked with a '$*$' symbol. The distance d is calculated using the *Gaia* DR3 (Gaia Collaboration et al. 2023) parallax.

Star	α_{J2000} (^{h} ^{m} ^{s})	δ_{J2000} ($^\circ$ $'$ $''$)	V ($\pm$0.01 mag)	A_V ($\pm$0.001 mag)	M_v ($\pm$0.01 mag)	d ($\pm$1 pc)	$T_{\rm eff}$ ($\pm$250 K)	$\log g$ ($\pm$0.20 dex)	[M/H] ($\pm$0.20 dex)	$\log(L/L_\odot)$ ($\pm$0.10 dex)
HD 23734	03 48 10.59	+21 19 44.66	7.96	0.086	2.56	120	7623[1]	4.09[1]	0.12[1]	0.89
							7700[2]	-	-	
							7660*	4.09*	0.12*	
HD 68703	08 14 11.14	+17 40 33.43	6.47	0.025	1.55	96	7340[1]	3.86[1]	0.32[1]	1.29
							7180[2]	-	-	
							7180[3]	4.02[3]	0.32[3]	
							7230*	3.93*	0.32*	
HD 73345	08 38 37.86	+19 59 23.09	8.14	0.039	1.82	184	7710[1]	3.99[1]	0.26[1]	1.16
							7300[2]	-	-	
							7980[3]	4.49[3]	0.25[3]	
							7660*	4.24*	0.26*	

[1] $uvby\beta$.
[2] 2MASS.
[3] Geneva.

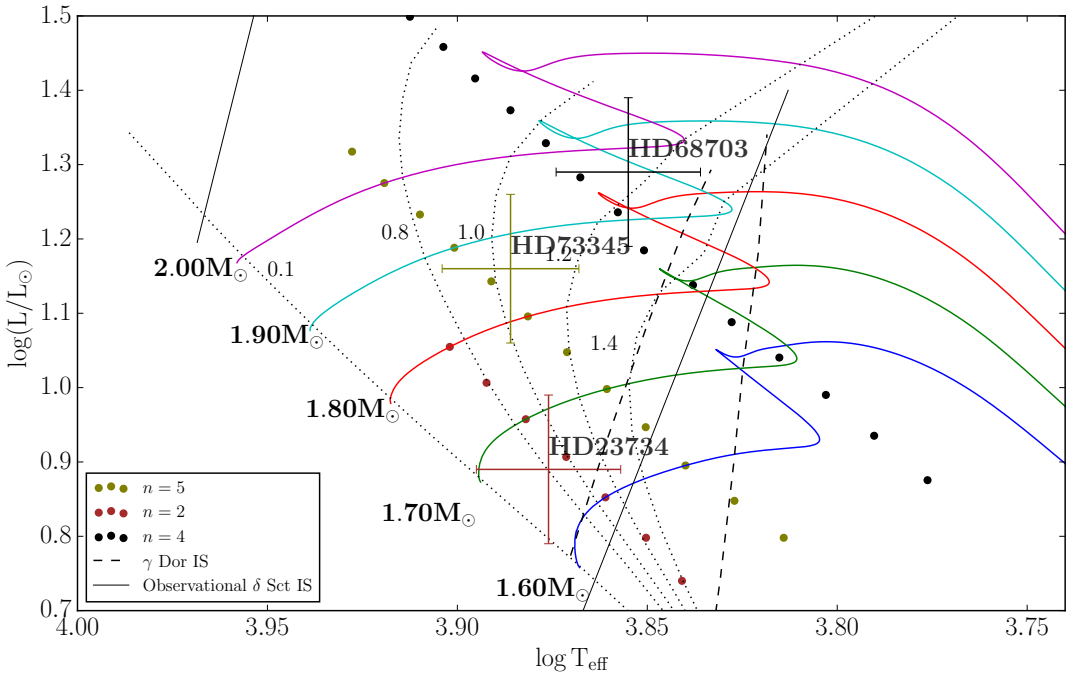

Figure 6. The evolutionary tracks encompasing mass range of 1.60 $M_\odot$ to 2.00 $M_\odot$, with solar metallicity ($Z = 0.014$) and $\alpha_{ov} = 0.1$. The dotted lines are the isochrones of ages 0.1, 0.8, 1.0, 1.2 and 1.4 Gyrs. The *black solid* lines are the observational δ Sct instability strip while the *black dashed* lines are the γ-dor instability strip. The scattered dots aligned with the ZAMS line represent the least seismic-χ^2 models for the radial overtones of $n = 2, 4$, and 5 for the stars HD 23734, HD 68703, and HD 73345, respectively, corresponding to the dominant frequency associated with each mass value.

Table 7. Stellar parameters for the stars HD 23734, HD 68703, and HD 73345 derived using spectroscopy.

Star	$T_{\rm eff}$ (±320 K)	log g (±0.30 dex)	$\xi_{\rm mic}$ (±1.0 km s^{-1})	[M/H] (±0.30)
HD 23734	7520	3.89	3.2	−0.20
HD 68703	7170	3.09	3.3	0.04
HD 73345	7690	3.10	2.7	−0.02

Table 8. Individual chemical abundances determined for our target stars from HESP spectra. The final column lists the solar abundances (Asplund et al. 2021; Magg et al. 2022). The values are presented as log $N_{\rm el}/N_{\rm tot}$. The typical error σ(log $N/N_{\rm tot}$) is comparable with 0.4-0.6 dex, excepting less accurate values marked by (:).

	HD 23734	HD 68703	HD 73345	Sun
Na	−5.49	−5.80	−5.53	−5.81
Mg	−4.48	−4.50 (:)	−4.18	−4.48
Ca	−5.82	−5.83	−5.78	−5.66
Sc	−9.43	−8.79	−9.21	−8.89
Ti	−7.36	−7.11	−7.19	−7.06
V	−7.66 (:)	−7.97 (:)	−8.31 (:)	−8.13
Cr	−6.39	−6.50	−6.58	−6.41
Mn	−7.21 (:)	−6.93	−6.63 (:)	−6.61
Fe	−4.77	−4.78	−4.65	−4.52
Ni	−6.28	−5.82	−5.72	−5.79
Zn	-	-	−7.15	−7.47
Y	-	−9.68	−9.96	−8.82
Zr	-	−9.20	−9.53	−9.44
Ba	−10.13	−9.42	−9.77	−9.76

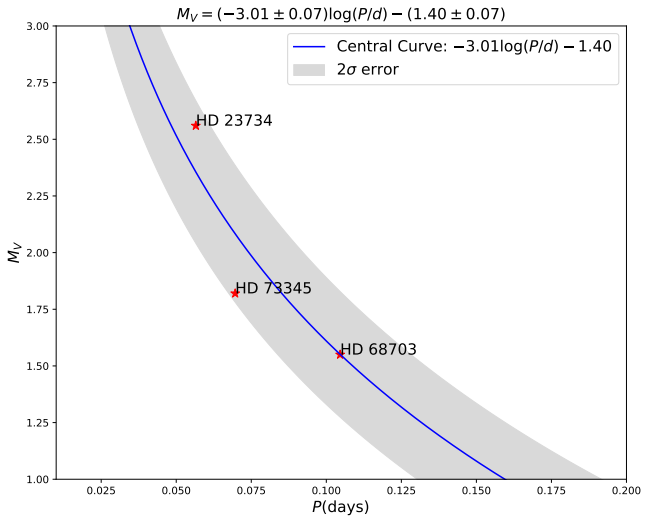

Figure 7. The solid curve represents the P-L relation of δ Sct stars proposed by Barac et al. (2022). The positions of the stars (marked in *star* symbol) are corresponding to their fundamental mode frequencies that lies within the shaded region corresponding to 2σ error region.

From the échelle diagram and seismic models (see following sub-sections), the fundamental mode is predicted at 17.69 d^{-1}(see Table 10). All the identified fundamental mode frequencies for three stars are within the 2σ level of the period-luminosity relation (see Fig. 7).

4.2 Échelle Diagram

The Échelle diagram (ED) is a key tool in asteroseismology for analyzing the pulsation modes. ED organizes the observed frequencies into segments of similar angular degree (ℓ) given a choice of large frequency separation ($\Delta\nu$). The frequencies associated with low-degree (ℓ<2) and high-order (for $n >> \ell$) pressure modes approximately follow the asymptotic relation (Tassoul 1980) given by,

$$\nu_{n,\ell} = \Delta\nu(n + \ell/2 + \epsilon) \tag{2}$$

where $n = 1, 2, 3, ...$ are the radial order of pulsation for a specific angular degree (ℓ), and ϵ is a constant of order unity. In the regime of higher radial orders (at large n), the spacing between two consecutive modes of the same angular degree approaches a constant (Bedding et al. 2020) or the modes are equally spaced. The large frequency separation ($\Delta\nu$) for δ Sct stars is the average spacing between consecutive radial modes (n) of the same spherical degree (ℓ) in their frequency spectrum. This $\Delta\nu$ of a star is related to it's mean density ($\bar{\rho}$) by the empirical relation (Suárez et al. 2014),

$$\frac{\Delta\nu}{\Delta\nu_\odot} = 0.776 \left(\frac{\bar{\rho}}{\bar{\rho}_\odot}\right)^{0.46} \tag{3}$$

where $\Delta\nu_\odot (= 135\mu Hz \approx 11.67 d^{-1})$ (Huber et al. 2011) and $\bar{\rho}_\odot$ are the solar large frequency separation and the mean density, respectively. In order to obtain an initial estimate of $\Delta\nu$, we calculated the mean density ($\bar{\rho}$) from stellar radii (R) and masses (M) derived using the Stefan-Boltzmann law ($L \propto R^2 T_{\rm eff}^4$) and theoretical isochrones, respectively; then the mean density is given by (M/R^3) (see Table 9). With these values, we optimized the value of $\Delta\nu$, using the dynamic échelle interface developed by Hey & Ball (2022). The échelle optimized values of $\Delta\nu$(ED) for HD 23734, HD 63345 and HD 73345 were determined to be 5.90 d^{-1}, 3.25 d^{-1} and 4.80 d^{-1}, respectively (see Fig. 8). For comparison, in Table. 9, we also list the updated mean densities determined from $\Delta\nu$(ED). The radial modes marked in the échelle diagram were refined with the theoretical model frequencies calculated in the next section.

4.3 Stellar Models

We adopted an iterative approach to determine the radial modes of the star with theoretical models. Our first assumption was the highest amplitude frequencies ($\nu_{\rm max}^{\rm radial}$) to be radial with some arbitrary order (n). Thus we calculated the stellar models for mass ranging from $1.40 - 2.20 M_\odot$ and for solar metallicity ($Z = 0.014$) with an overshooting ($\alpha_{\rm ov} = 0.1$), using the stellar evolution code CLÉS (Code Liégeois d'Evolution Stellaire; Scuflaire et al. 2008a). Then, we generated the overtones for radial mode ($\ell = 0$) using stellar oscillation code (OSC: Scuflaire et al. (2008b)) with different choices of n for $\nu_{\rm max}^{\rm radial}$. We selected the best n by performing a seismic fit for the identified radial modes with each choice of n values. For seismic fit, we calculated the seismic-χ^2 values given by (Murphy et al. 2021),

$$\chi^2 = \left(\frac{F_t - F_o}{\sigma_{F,o}}\right)^2 \tag{4}$$

F_t and F_o are the model and observed frequencies of the identified radial mode, respectively, and here $\sigma_{F,o}$ is considered 0.1 (Murphy et al. 2021). The best fit model was then used to determine the seismic parameters of the stars by plotting the models for different choices of masses in the HR diagram (see the scatter plots in Fig. 6). We constrained the mass range of the stars in the HR diagram as 1.65, 1.95 and $1.85 M_\odot$ (± 0.10) for the stars HD 23734, HD 68703 and HD 73345, respectively.

4.4 Frequency Ratios

Further, we used the Petersen Diagram (Petersen 1973, 1978) for p-mode pulsating variables that plots the ratio of the frequencies of the star's radial overtones to its fundamental radial mode. Here, we took the ratios of the theoretical radial overtones ($n \geq 2$) to different choices of fundamental mode frequency ($n = 1$) and plotted them in Fig. 9. We compare the theoretical frequency ratios with the ratios of radial modes identified based on the observed frequencies. In the flat region of the Petersen diagram (i.e. here nearly > 9 d^{-1}), there is very small dependence on the overshooting parameter ($\alpha_{\rm ov}$) and its effect can be ignored (Sarkar et al. 2024). These ratios confirm the choice of mode selection in the previous section.

4.5 Pulsation Constant (Q-values)

Finally, the identified radial modes for the stars are further verified by calculating the pulsation constant (Q-values) for identified radial modes using the mean density relation and the theoretically predicted Q-values. The relation between Q-value and the mean density is given by

$$Q = \frac{1}{f}\sqrt{\frac{\bar{\rho}}{\bar{\rho}_\odot}} \tag{5}$$

The Q-values for the stars HD 23734, HD 68703 and HD 73345 are calculated using Eq. 5 and mentioned in Table 2, 3 and 4 respectively. We then calculated the Q-values from the seismic models using theoretical radial overtone frequencies (f) and mean density ($\bar{\rho}$) at each step of the evolutionary track and plotted them against the theoretical radial overtones (f) (see Fig. 10). However, there is variation with stellar mass as the Q-values increase; as mass increases, the slope of the Q-value curve exhibits a steeper trend and settles at lower values with increasing frequency. A comparison of the calculated Q-values for the three stars is presented for three distinct mass values associated with each star, as indicated in Table 9. The errors associated with the mass estimations (± 0.05) exert a minimal influence on the Q-value curve ($\sim 10^{-3}$) and do not indicate any discrepancies in the results of the mode identification.

5 RESULTS AND DISCUSSION

The present study aims to determine reliable fundamental parameters of three multiperiodic pulsating variables to carry out asteroseismic studies. In the following subsections, we summarize the results obtained on the individual star :

5.1 HD 23734 (EPIC 210895951 or TIC 440687375)

Frequency analysis of the 2-min cadence time-series *TESS* photometric data obtained on the three consecutive sectors (42, 43, 44) for HD 23734 resulted a total of 28 independent frequencies and 36 combination or harmonic frequencies. A rotational frequency ($F_{\rm rot}$ = 2.3406 d^{-1}) was also detected, although with low amplitude peak which is in agreement with the stellar radii and $\upsilon \sin i$ also showing several harmonics and combinations. Only three frequencies are in

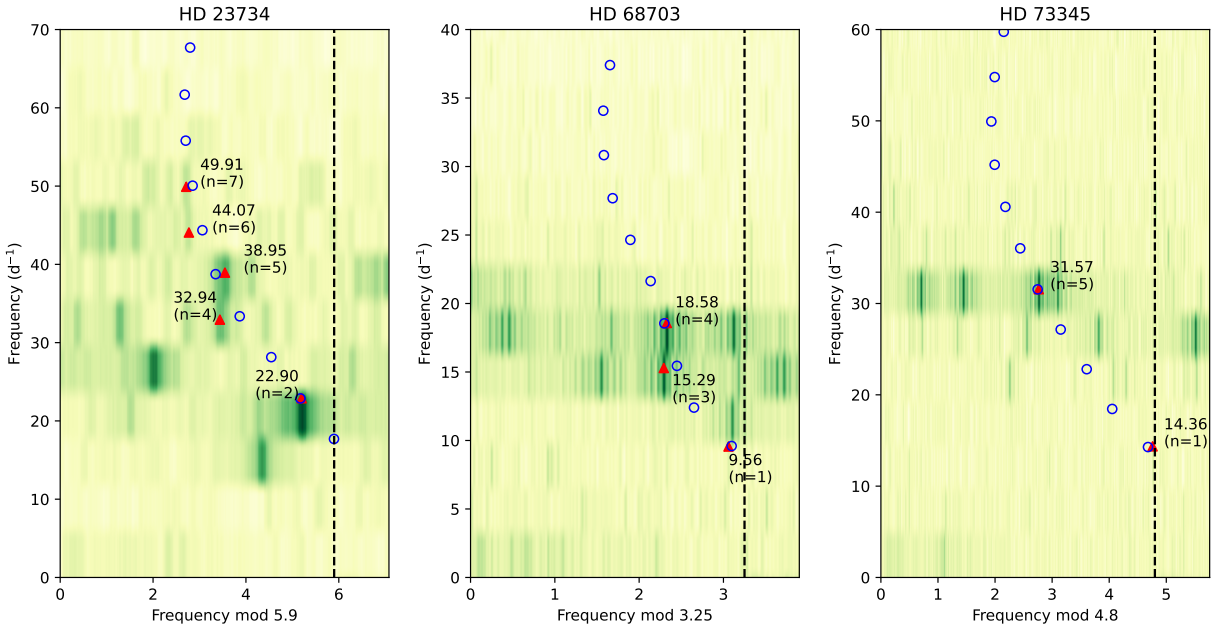

Figure 8. Échelle diagrams of HD 23734, HD 68703, and HD 73345 produced for the calculated large frequency separation 5.90, 3.25 and 4.80 d^{-1} respectively. The black dashed lines are at large separation ($\Delta\nu$). The portion beyond this line is 20 percent of the échelle diagram that is repeated for clarity. The radial modes computed from the seismic models are represented by empty circles, while the filled triangles belong to observed radial modes.

Table 9. The frequency of the observed radial overtone of highest amplitude $\nu^{\rm max}_{\rm radial}$, the large frequency separation calculated from mean density relation ($\Delta\nu$), from the dynamic échelle diagram, the radial order (n), the mean density ($\bar{\rho}$) from luminosity, mean density from the large separation from ED, the radius of the star R_L from Stefan-Boltzmann relation, fundamental mode (f_0), the ratio $f_0/3\Delta\nu$, pulsation Q-value and stellar mass M estimated from the isochrones.

Star	$\nu^{\rm radial}_{\rm max}$ (d^{-1})	$\Delta\nu$ (d^{-1})	$\Delta\nu$ (ED) (d^{-1})	n	$\bar{\rho}/\bar{\rho}_\odot$ [Luminosity]	$\bar{\rho}/\bar{\rho}_\odot$ [ED]	$R_L/R_\odot$	f_0 (cal) (d^{-1})	$f_0/3\Delta\nu$	Q (days) (±0.0010)	$M/M_\odot$ (isochrone) (±0.10)
HD 23734	22.90	5.78 ± 1.02	5.90	2	0.373 ± 0.143	0.66	1.64 ± 0.21	17.69*	0.97*	0.0267	1.65
HD 68703	18.57	2.91 ± 0.51	3.25	4	0.0835 ± 0.0323	0.12	2.86 ± 0.37	9.56	0.98	0.0155	1.95
HD 73345	31.56	4.52 ± 0.66	4.80	5	0.2186 ± 0.0700	0.26	2.15 ± 0.27	14.36	0.99	0.0148	1.85

* Not observed value but calculated from the best-fit model.

Table 10. The radial overtones for different radial orders (n) for the best-fit model calculated using metallicity values ($Z = 0.014$) and with overshooting parameter $\alpha_{ov} = 0.1$ for the stars HD 23734, HD 68703 and HD 73345.

	Frequency (d^{-1})		
n	HD 23734	HD 68703	HD 73345
1	17.69	9.59	14.27
2	22.87	12.40	18.45
3	28.14	15.44	22.80
4	33.36	18.54	27.15
5	38.74	21.63	31.54
6	44.36	24.64	36.04
7	50.05	27.68	40.58
8	55.80	30.83	45.19
9	61.68	34.07	49.93
10	67.69	37.40	54.79

common with the *K2* dataset. Through mode identification, we identified five radial orders ($n = 2, 4, 5, 6$, and 7), while the fundamental radial order is not detected in TESS. The large frequency separation is found to be 5.90 d^{-1}using échelle diagram, which is consistent with the large separation from the mean density calculation. The results of our combined spectroscopic and photometric study portray HD 23734 as a δ Sct star with solar composition. The combination of calculated asteroseismic models and observed parameters resulted in the age and mass of this star being 0.989 Gyrs and 1.65 $M_\odot$, respectively. These findings are in consistent to the value estimated from the HR diagram. The RV variations from available spectra show a variation not typical for pulsational variations and are possibly due to binarity and this fact can be confirm through the additional observations.

5.2 HD 68703 (EPIC 211825317 or TIC 27652512)

HD 68703 was classified as F1IV spectral type star (Barry 1970; Abt & Morrell 1995). Based on multicolour photometry, it was suspected to be an Am star by Cowley & Crawford (1971). This star islisted in the general catalogue of Ap and Am stars (Renson & Manfroid 2009). HD 68703 was observed by *K2* and *TESS* missions in both the long and short cadences. The frequency spectra show a low-frequency peak at 1.0995 d^{-1}along with multiple harmonics

Table 11. A comparison between atmospheric parameters estimated from best-fit models and observations.

	Seismic best-fit			Observational		
Name	$\log(L/L_\odot)$	$\log T_{\rm eff}$	Age (Gyr)	$\log(L/L_\odot)$ (±0.10)	$\log T_{\rm eff}$ (±0.02)	Age (Gyr)
HD 23734	0.880	3.896	0.989	0.89	3.88	0.8
HD 68703	1.175	3.854	1.290	1.29	3.86	1.2
HD 73345	1.143	3.854	0.980	1.16	3.89	1.0

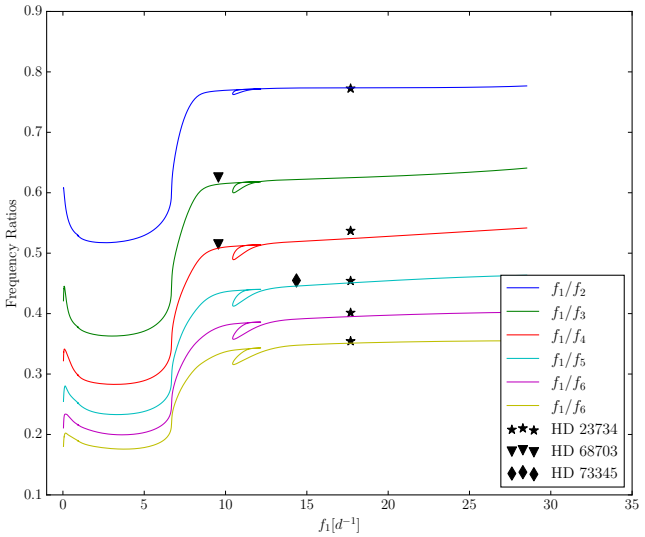

Figure 9. The theoretical Peteresen diagram (*solid lines*) calculated for $Z = 0.014$ and $\alpha_{\rm ov} = 0.1$. The X-axis represents the fundamental mode frequency (f_0) and the Y-axis is the frequency ratios of the fundamental mode to the consecutive overtones. The scatter points are the frequency ratios corresponding to the radial modes identified from the échelle diagram and show a good agreement.

and hence it is identified as a rotational frequency. Apart from the identified rotational frequency, a total of 21 independent frequencies were extracted with 16 combinations of the rotational frequency or radial modes. Interestingly, two frequencies of significant amplitude in the *K2* data is absent in the *TESS* data that is a clear evidence of the wavelength dependence of pulsational frequency. We found the fundamental, third and fourth radial overtones in the star, where the fourth overtone dominates the frequency spectrum. The large frequency separation is determined to be 3.25 $\rm d^{-1}$. On comparison of the amplitude spectra of the individual time-series data, the amplitude modulation is also seen for some of the frequencies that could be due to the presence of spots on the stellar surface and/or beating of the close pulsational frequencies, but this needs separate investigation which is out of the scope of the present study. Considering the rotational frequency and projected rotational velocity $\upsilon \sin i$ as input parameters, we constrain the inclination angle of the star as $i \approx 25°$. On inspecting the LSD profile of the spectral lines, we notice a clear line profile variations those are found in the multi-periodic pulsating variables. The detailed abundance analysis shows that all the investigated elements are near solar values, hence classified as a normal star. The results of the medium-resolution spectropolarimetry published by Kudryavtsev et al. (2006) show HD 68703 as a non-magnetic star and same conclusion is drawn based on the analysis of the high-resolution spectroscopy with NARVAL, a spectropolarimeter of the 2.0-m Telescope Bernard Lyot (TBL), is given in the Polarbase[7] database Petit et al. (2014). Owing to the intriguing photometric and spectroscopic peculiarities, HD 68703 is an ideal candidate for further asteroseismic investigation using a combined photometric and spectroscopic approach.

5.3 HD 73345 (EPIC 211983602 or TIC 175194881)

The star HD 73345, shows 19 independent frequencies those were retrieved from the time-series data. Among them, 4 frequencies are detected in *K2* but not in *TESS*. Similarly, 10 frequencies that were recorded in the *TESS* data are absent in the *K2* data, again the observing wavelength dependence of frequencies will be at play. We identified the fundamental and fifth radial overtones, with the dominant mode being the 5^{th} overtone. The pulsation spectrum and the position in the HR diagram indicate that HD 73345 is a δ Sct pulsator. In the frequency spectrum of *TESS* data, a significant peak is visible at frequency $f = 1.1119\,\rm d^{-1}$ which may be attributed to rotation, but we did not find any harmonics of this posible rotational frequency. We interpreted this as rotational frequency because it is in agreement with the stellar radius and $\upsilon \sin i$ and also shows combinations with radial orders. The abundance analysis of this star revealed that all the elements are near solar values and, hence HD 73345 can be classified as a normal A-F type pulsator.

The large frequency separation is determined to be $4.80 d^{-1}$ using the échelle diagram, which aligns with the large separation derived from mean density calculations. However, HD 73345 is classified as a δ Sct star and a member of the group *Praesepe* and has an estimated large frequency separation of $\Delta\nu_{low} = 52\mu Hz$ (Pamos Ortega et al. 2023) ($\approx 4.49 d^{-1}$). For the seismic analysis of the star in *Praesepe* they used metallicity in the range [0.028,0.032] and included the rotation Ω/Ω_c=[0.1,0.5]. Our results shows an overestimation of the seismic age of nearly a Gyr, whereas the literature value suggests around 470 ± 120 Myrs (Pamos Ortega et al. 2023). This discrepancy could be attributed due to the effect of rotation. As rotation in a star extends its lifespan due to the transfer of fresh hydrogen. The star's position in the HR diagram indicates proximity to the TAMS phase. The RV variations are greater than those expected for pulsations, so the star could be part of a binary system. But this need confirmation by acquiring more data to cover the phase space of variations.

6 CONCLUSIONS AND FUTURE PROSPECTS

The primary objective of the extension of the ongoing N-C survey is to gain insights into the interaction between stellar activities such as

[7] PolarBase: A Database of High-Resolution Spectropolarimetric Stellar Observations. http://polarbase.irap.omp.eu/

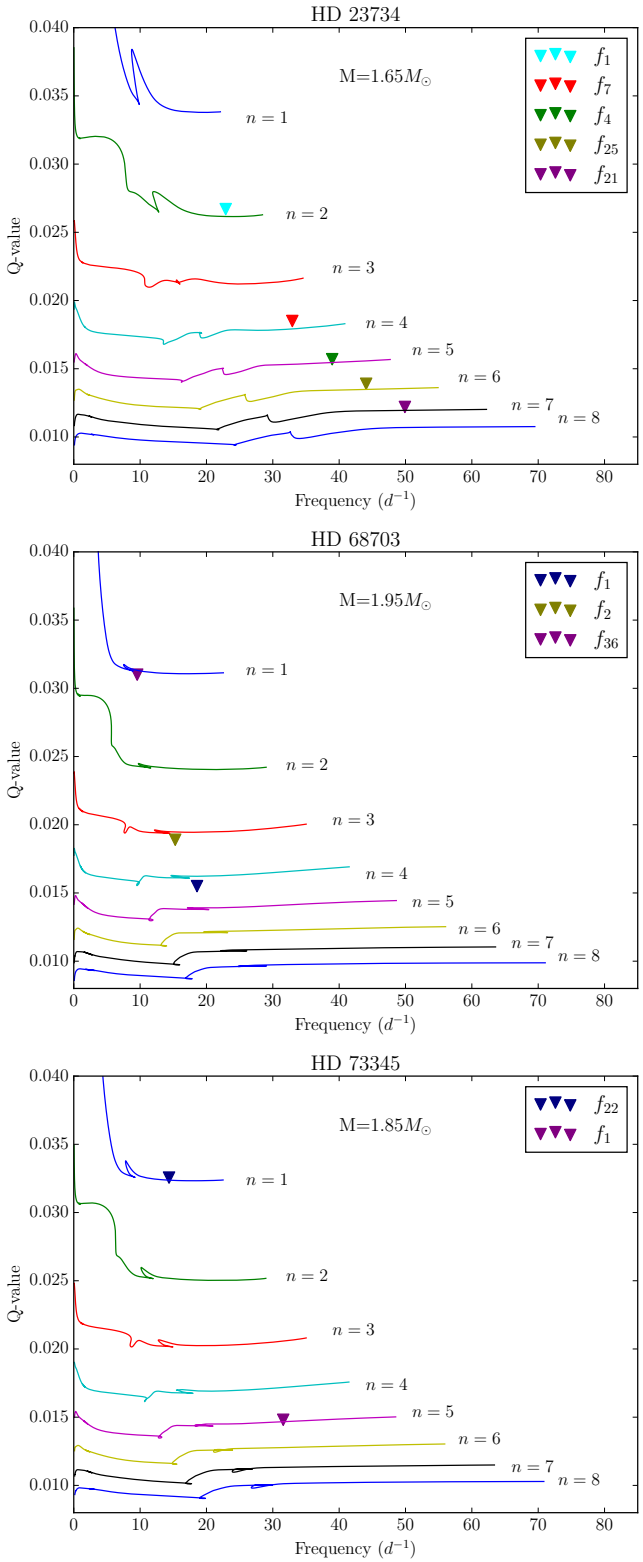

Figure 10. Theoretical Q-value curves for the masses 1.65, 1.95 and 1.85$M_\odot$ for the stars HD 23734, HD 68703 and HD 73345, respectively. The frequency IDs mentioned in the legend are the frequency numbers of the identified radial modes of the corresponding star. The scatter points correspond to the frequencies that are identified radial modes and are found consistent.

pulsation, chemical inhomogeneities, rotation, magnetic fields using data acquired from state-of-the-art instruments attached to ground- and space-based telescopes to perform the asteroseismic study of the pulsating variables located on or near the MS of the HR diagram.

Based on the current investigation, we derive the following conclusions:

(i) Through the exploitation of the *K2* and *TESS* photometry, we found that HD 23734, HD 68703, and HD 73345 are multi-periodic pulsating variables though they were previously classified as non-pulsators based on the ground-based observations. Therefore, we have demonstrated that it is worthwhile to re-examine the variability and peculiarity classification of all the objects previously announced as null results under the N-C survey with high-resolution photometry and spectroscopy, respectively.

(ii) We were able to determine the basic astrophysical parameters using the high-resolution spectroscopy to use them as input for modeling. Our finding from the evaluation of the chemical abundances is that all the studied stars appear to be normal A- and F-type stars. A more accurate peculiar categorization can be done on the magnetic measurements through the spectropolarimetric observations in the case of HD 23734 and HD 73345.

(iii) The LSD profiles of one of the targets, HD 68703 show notable line profile variations rendering this star an ideal candidate for the follow-up time-series spectroscopic studies for a detailed investigation to study the interaction of the rotation and pulsation.

(iv) The position of the targets in the HR diagram and their seismic ages indicate that the star HD 23734 is located in the ZAMS phase and has commenced core H burning. Similarly, HD 68703 is approaching to the TAMS where the core H is about to run out. The star HD 73345 is found in the MS phase where the H fusion is still going on.

(v) We followed independent approaches to identify and validate the several excited radial modes. The period-luminosity relation was used to identify the fundamental modes while the radial overtones were identified using the échelle diagrams, pulsation models, the Petersen diagrams.

(vi) Our investigation of binarity resulted that HD 23734 and HD 73345 are likely to be binary stars, albeit the phase coverage restricted their characteristics, and requires additional RV measurements for the confirmation and further investigation. For HD 68703, the available RV data did not secure the presence of any binarity component.

The present study can further employ additional approaches to discover the non-radial modes for the studied stars. We have identified many interesting targets monitored under the N-C Survey and are also observed by *TESS* data and will continue to investigate them in near future for their pulsations in the presence of rotation, binarity and chemical peculiarities.

DATA AVAILABILITY STATEMENT

The high-resolution spectroscopic data used in this article will be shared on reasonable request by the corresponding author. TESS time-series flux of the target stars is available on NASA's MAST website. This work has made use of data from the European Space

Agency (ESA) mission Gaia (https://www.cosmos.esa.int/gaia), processed by the Gaia Data Processing and Analysis Consortium (DPAC, https://www.cosmos.esa.int/web/gaia/dpac/consortium). Funding for the DPAC has been provided by national institutions, in particular the institutions participating in the Gaia Multilateral Agreement. This research has made use of the SIMBAD database, operated at CDS, Strasbourg, France.

REFERENCES

Abt H. A., Morrell N. I., 1995, ApJS, 99, 135
Abt H. A., Snowden M. S., 1973, ApJS, 25, 137
Aerts C., Christensen-Dalsgaard J., Kurtz D. W., 2010, Asteroseismology. Springer
Antoci V., et al., 2014, ApJ, 796, 118
Asplund M., Grevesse N., Sauval A. J., Scott P., 2009, ARA&A, 47, 481
Asplund M., Amarsi A. M., Grevesse N., 2021, A&A, 653, A141
Aurière M., et al., 2007, A&A, 475, 1053
Babcock H. W., 1947, ApJ, 105, 105
Baker N., Kippenhahn R., 1962, Zeitschrift für Astrophysik, 54, 114
Balona L. A., 2022, arXiv e-prints, p. arXiv:2212.10776
Barac N., Bedding T. R., Murphy S. J., Hey D. R., 2022, MNRAS, 516, 2080
Baran A. S., Koen C., Pokrzywka B., 2015, MNRAS, 448, L16
Barry D. C., 1970, ApJS, 19, 281
Bedding T. R., et al., 2020, Nature, 581, 147
Braithwaite J., Spruit H. C., 2004, Nature, 431, 819
Breger M., 1970, ApJ, 162, 597
Breger M., 1990, Delta Scuti Star Newsletter, 2, 13
Bryson S. T., et al., 2010, ApJ, 713, L97
Buzasi D. L., et al., 2005, ApJ, 619, 1072
Bychkov V. D., Bychkova L. V., Madej J., 2021, Astronomical and Astrophysical Transactions, 32, 137
Casagrande L., et al., 2021, MNRAS, 507, 2684
Catanzaro G., Busà I., Gangi M., Giarrusso M., Leone F., Munari M., 2019, MNRAS, 484, 2530
Chanumolu A., Jones D., Thirupathi S., 2015, Experimental Astronomy, 39, 423
Conti P. S., 1970, PASP, 82, 781
Cowley A. P., Crawford D. L., 1971, Publications of the Astronomical Society of the Pacific, 83, 296
Cox A. N., 2000, Allen's astrophysical quantities. Springer
Crawford D. L., Mander J., 1966, AJ, 71, 114
Cui X.-Q., et al., 2012, Research in Astronomy and Astrophysics, 12, 1197
Cutri R. M., et al., 2003, VizieR Online Data Catalog, p. II/246
Dileep A., Joshi S., Kurtz D. W., 2024, Bulletin de la Societe Royale des Sciences de Liege, 93, 227
Dileep A., et al., 2025, Monthly Notices of the Royal Astronomical Society, 538, 1747
Donati J.-F., Brown S. F., 1997, A&A, 326, 1135
Dupret M. A., Grigahcène A., Garrido R., Gabriel M., Scuflaire R., 2004, A&A, 414, L17
Dürfeldt-Pedros O., Antoci V., Smalley B., Murphy S., Posilek N., Niemczura E., 2024, A&A, 690, A104
Gaia Collaboration 2018, VizieR Online Data Catalog, p. I/345
Gaia Collaboration et al., 2016, A&A, 595, A2
Gaia Collaboration et al., 2023, A&A, 674, A1
Ghazaryan S., Alecian G., 2016, MNRAS, 460, 1912
Ghazaryan S., Alecian G., Hakobyan A. A., 2018, MNRAS, 480, 2953
Golay M., 1980, Vistas in Astronomy, 24, 141
Green G. M., 2018, JOSS, 3, 695
Green G. M., Schlafly E. F., Zucker C., Speagle J. S., Finkbeiner D. P., 2019, arXiv e-prints, p. arXiv:1905.02734
Guzik J. A., 2021, Frontiers in Astronomy and Space Sciences, 8, 55
Guzik J. A., Jackiewicz J., Catanzaro G., Soukup M. S., 2021, in Posters from the TESS Science Conference II (TSC2). p. 38, doi:10.5281/zenodo.5121878
Hauck B., Mermilliod M., 1998, A&AS, 129, 431
Hey D., Ball W., 2022, Echelle: Dynamic echelle diagrams for asteroseismology, Astrophysics Source Code Library, record ascl:2207.005
Holdsworth D. L., et al., 2021, MNRAS, 506, 1073
Holdsworth D. L., et al., 2024, MNRAS, 527, 9548
Howell S. B., et al., 2014, PASP, 126, 398
Huber D., et al., 2011, ApJ, 743, 143
Iliev I. K., Budaj J., 2008, Contributions of the Astronomical Observatory Skalnate Pleso, 38, 129
Joshi S., Joshi Y. C., 2015, Journal of Astrophysics and Astronomy, 36, 33
Joshi S., et al., 2003, MNRAS, 344, 431
Joshi S., Mary D. L., Martinez P., Kurtz D. W., Girish V., Seetha S., Sagar R., Ashoka B. N., 2006, A&A, 455, 303
Joshi S., Mary D. L., Chakradhari N. K., Tiwari S. K., Billaud C., 2009, A&A, 507, 1763
Joshi S., Ryabchikova T., Kochukhov O., Sachkov M., Tiwari S. K., Chakradhari N. K., Piskunov N., 2010, MNRAS, 401, 1299
Joshi S., et al., 2012, MNRAS, 424, 2002
Joshi S., et al., 2016, A&A, 590, A116
Joshi S., Semenko E., Moiseeva A., Sharma K., Joshi Y. C., Sachkov M., Singh H. P., Yerra B. K., 2017, MNRAS, 467, 633
Joshi S., et al., 2022, MNRAS, 510, 5854
Krtička J., Janík J., Marková H., Mikulášek Z., Zverko J., Prvák M., Skarka M., 2013, A&A, 556, A18
Kudryavtsev D. O., Romanyuk I. I., Elkin V. G., Paunzen E., 2006, MNRAS, 372, 1804
Kunzli M., North P., Kurucz R. L., Nicolet B., 1997, A&AS, 122, 51
Kupka F. G., Ryabchikova T. A., Piskunov N. E., Stempels H. C., Weiss W. W., 2000, Baltic Astronomy, 9, 590
Kurtz D. W., 1976, ApJS, 32, 651
Kurtz D. W., Saio H., Holdsworth D. L., Joshi S., Seetha S., 2024, MNRAS, 529, 556
Lallement R., Vergely J. L., Babusiaux C., Cox N. L. J., 2022, A&A, 661, A147
Lampens P., et al., 2013, A&A, 549, A104
Lenz P., Breger M., 2005, CoAst, 146, 53
Lightkurve Collaboration et al., 2018, Lightkurve: Kepler and TESS time series analysis in Python, ascl soft (ascl soft:1812.013)
Loumos G. L., Deeming T. J., 1978, Ap&SS, 56, 285
Magg E., et al., 2022, A&A, 661, A140
Martinez P., et al., 2001, A&A, 371, 1048
Michaud G., 1970, ApJ, 160, 641
Mikulášek Z., Krtička J., Henry G. W., de Villiers S. N., Paunzen E., Zejda M., 2010, A&A, 511, L7
Montgomery M. H., O'Donoghue D., 1999, Delta Scuti Star Newsletter, 13, 28
Moon T. T., Dworetsky M. M., 1985, MNRAS, 217, 305
Murphy S. J., Hey D., Van Reeth T., Bedding T. R., 2019, MNRAS, 485, 2380
Murphy S. J., Joyce M., Bedding T. R., White T. R., Kama M., 2021, MNRAS, 502, 1633
Napiwotzki R., Schoenberner D., Wenske V., 1993, A&A, 268, 653
Pamos Ortega D., Mirouh G. M., García Hernández A., Suárez Yanes J. C., Barceló Forteza S., 2023, A&A, 675, A167
Paunzen E., 2015, A&A, 580, A23
Paunzen E., 2022, A&A, 661, A89
Paunzen E., 2024, in de Grijs R., Whitelock P. A., Catelan M., eds, IAU Symposium Vol. 376, IAU Symposium. pp 91–97, doi:10.1017/S1743921323003538
Paunzen E., Supíková J., Bernhard K., Hümmerich S., Prišegen M., 2021, MNRAS, 504, 3758
Petersen J. O., 1973, A&A, 27, 89
Petersen J. O., 1978, A&A, 62, 205
Petit P., Louge T., Théado S., Paletou F., Manset N., Morin J., Marsden S. C., Jeffers S. V., 2014, PASP, 126, 469
Piskunov N., Valenti J. A., 2017, A&A, 597, A16
Piskunov N. E., Kupka F., Ryabchikova T. A., Weiss W. W., Jeffery C. S., 1995, A&AS, 112, 525
Poro A., et al., 2021, PASP, 133, 084201

Poznanski D., Prochaska J. X., Bloom J. S., 2012, MNRAS, 426, 1465
Preston G. W., 1974, ARA&A, 12, 257
Raskin G., et al., 2011, A&A, 526, A69
Renson P., Manfroid J., 2009, A&A, 498, 961
Richer J., Michaud G., Turcotte S., 2000, ApJ, 529, 338
Ricker G. R., et al., 2015, Journal of Astronomical Telescopes, Instruments, and Systems, 1, 014003
Rodríguez E., Breger M., 2001, A&A, 366, 178
Rufener F., Nicolet B., 1988, A&A, 206, 357
Ryabchikova T., Piskunov N., Kurucz R. L., Stempels H. C., Heiter U., Pakhomov Y., Barklem P. S., 2015, Phys. Scr., 90, 054005
Sarkar M., et al., 2024, MNRAS, 534, 3211
Scuflaire R., Théado S., Montalbán J., Miglio A., Bourge P. O., Godart M., Thoul A., Noels A., 2008a, Ap&SS, 316, 83
Scuflaire R., Montalbán J., Théado S., Bourge P. O., Miglio A., Godart M., Thoul A., Noels A., 2008b, Ap&SS, 316, 149
Shore S. N., Adelman S. J., 1974, ApJ, 191, 165
Smalley B., et al., 2017, MNRAS, 465, 1
Sriram S., et al., 2018, in Proc. SPIE. p. 107026K, doi:10.1117/12.2313165
Steindl T., Zwintz K., Müllner M., 2022, A&A, 664, A32
Strömgren B., 1963, QJRAS, 4, 8
Strömgren B., 1966, ARA&A, 4, 433
Suárez J. C., García Hernández A., Moya A., Rodrigo C., Solano E., Garrido R., Rodón J. R., 2014, A&A, 563, A7
Tassoul M., 1980, ApJS, 43, 469
Torres G., 2010, AJ, 140, 1158
Trust O., Jurua E., De Cat P., Joshi S., 2020, MNRAS, 492, 3143
Trust O., Jurua E., De Cat P., Joshi S., Lampens P., 2021, MNRAS, 504, 5528
Trust O., Mashonkina L., Jurua E., De Cat P., Tsymbal V., Joshi S., 2023, MNRAS, 524, 1044
Uytterhoeven K., et al., 2011, A&A, 534, A125
Valenti J. A., Piskunov N., 1996, A&AS, 118, 595
Vergely J. L., Lallement R., Cox N. L. J., 2022, A&A, 664, A174
Vernet J., et al., 2011, A&A, 536, A105
Wenger M., et al., 2000, A&AS, 143, 9
Zhao G., Zhao Y.-H., Chu Y.-Q., Jing Y.-P., Deng L.-C., 2012, Research in Astronomy and Astrophysics, 12, 723
Ziaali E., Bedding T. R., Murphy S. J., Van Reeth T., Hey D. R., 2019, MNRAS, 486, 4348
de Cuyper J. P., Hensberge H., Raskin G., van Winckel H., Lehmann H., Winkler J., Laux U., 2007, in Shaw R. A., Hill F., Bell D. J., eds, Astronomical Society of the Pacific Conference Series Vol. 376, Astronomical Data Analysis Software and Systems XVI. p. 653

ACKNOWLEDGMENTS

This work is supported by the Belgo-Indian Network for Astronomy and astrophysics (BINA), approved by the International Division, Department of Science and Technology (DST, Govt. of India; DST/INT/BELG/P-09/2017) and the Belgian Federal Science Policy Office (BELSPO, Govt. of Belgium; BL/33/IN12). SJ and OT acknowledge the financial support received from the BRICS grant DST/ICD/BRICS/Call-5/SAPTARISI/2023(G). AD acknowledges the financial support received from DST-INSPIRE Fellowship Programme (DST/INSPIREFellowship/2020/IF200245). OT acknowledge financial support from the International Science Programme (ISP) of Uppsala University and IP the use of SIMBAD, NASA's ADS and ESA's Hipparcos database. SJ, APY, and SP gratefully acknowledge the financial support from the Core Research Grant (CRG/2021/007772) of the Science and Engineering Research Board (SERB), India. This paper includes data collected by the *Kepler* mission available at Mikulski Archive for Space Telescopes (MAST) operated by NASA. Based on observations made with the Mercator Telescope, operated on the island of La Palma by the Flemish Community, at the Spanish Observatorio del Roque de los Muchachos of the Instituto de Astrofísica de Canarias. Based on observations obtained with the HERMES spectrograph, which is supported by the Research Foundation - Flanders (FWO), Belgium, the Research Council of KU Leuven, Belgium, the Fonds National de la Recherche Scientifique (F.R.S.-FNRS), Belgium, the Royal Observatory of Belgium, the Observatoire de Genève, Switzerland and the Thüringer Landessternwarte Tautenburg, Germany. Guoshoujing Telescope (the Large Sky Area Multi-Object Fiber Spectroscopic Telescope LAMOST) is a National Major Scientific Project built by the Chinese Academy of Sciences. Funding for the project has been provided by the National Development and Reform Commission. LAMOST is operated and managed by the National Astronomical Observatories, Chinese Academy of Sciences. The LAMOST spectra are avaialble at https://www.lamost.org/. Part of the research is based on data obtained from the European Southern Observatory(ESO) Science Archive Facility with DOI(s): https://doi.org/10.18727/archive/24, https://doi.eso.org/10.18727/archive/50, and https://doi.org/10.18727/archive/71 under ESO Prog ID 110.248M.001

This research has used data, tools or materials developed as part of the EXPLORE project that has received funding from the European Union's Horizon 2020 research and innovation programme under grant agreement No 101004214.

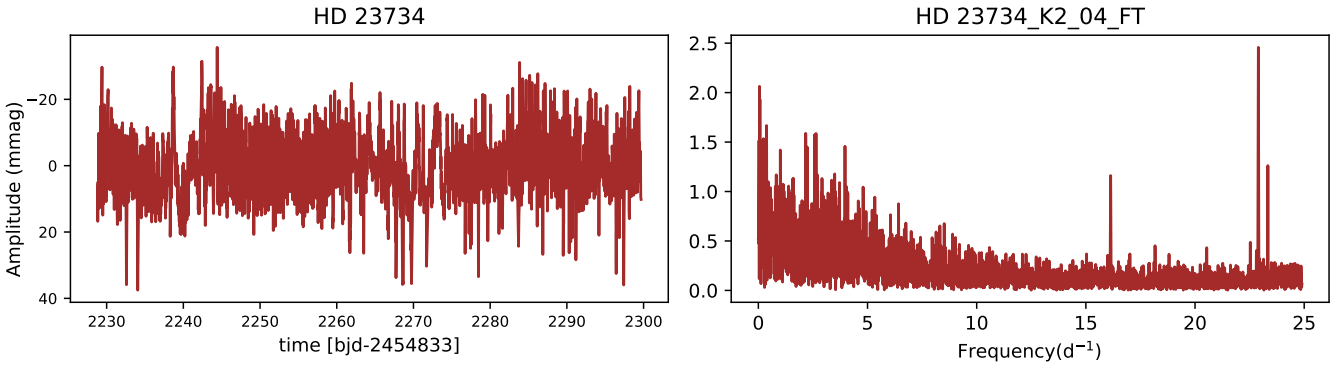

Figure A1. The light curve (left panel) and corresponding frequency spectrum (right panel) for HD 23734 obtained with *K2* in campaign 4.

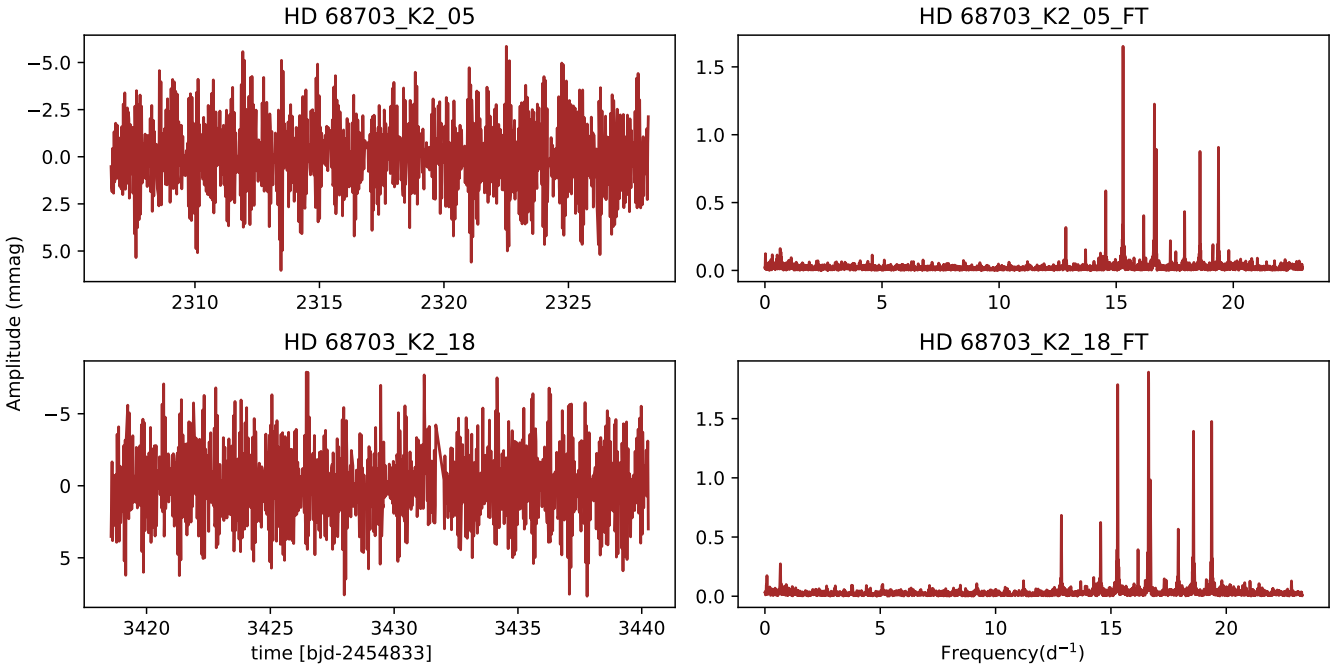

Figure A2. The light curves (left panels) and corresponding frequency spectra (right panels) for HD 68703 obtained with *K2* in campaign 5 (top row) and 18 (bottom row).

APPENDIX A: TESS AND K2 LIGHT CURVES.

This paper has been typeset from a TEX/LATEX file prepared by the author.

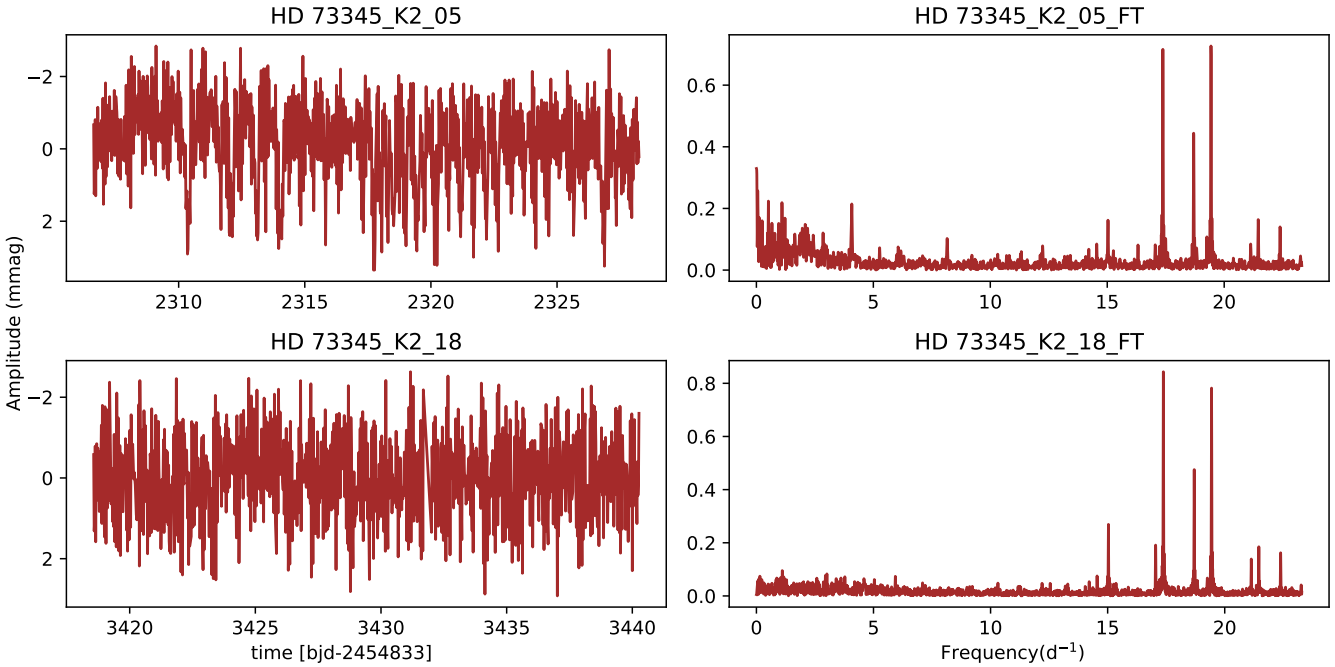

Figure A3. The light curves (left panels) and corresponding frequency spectra (right panels) for HD 73345 obtained with *K2* in campaign 5 (top row) and 18 (bottom row).

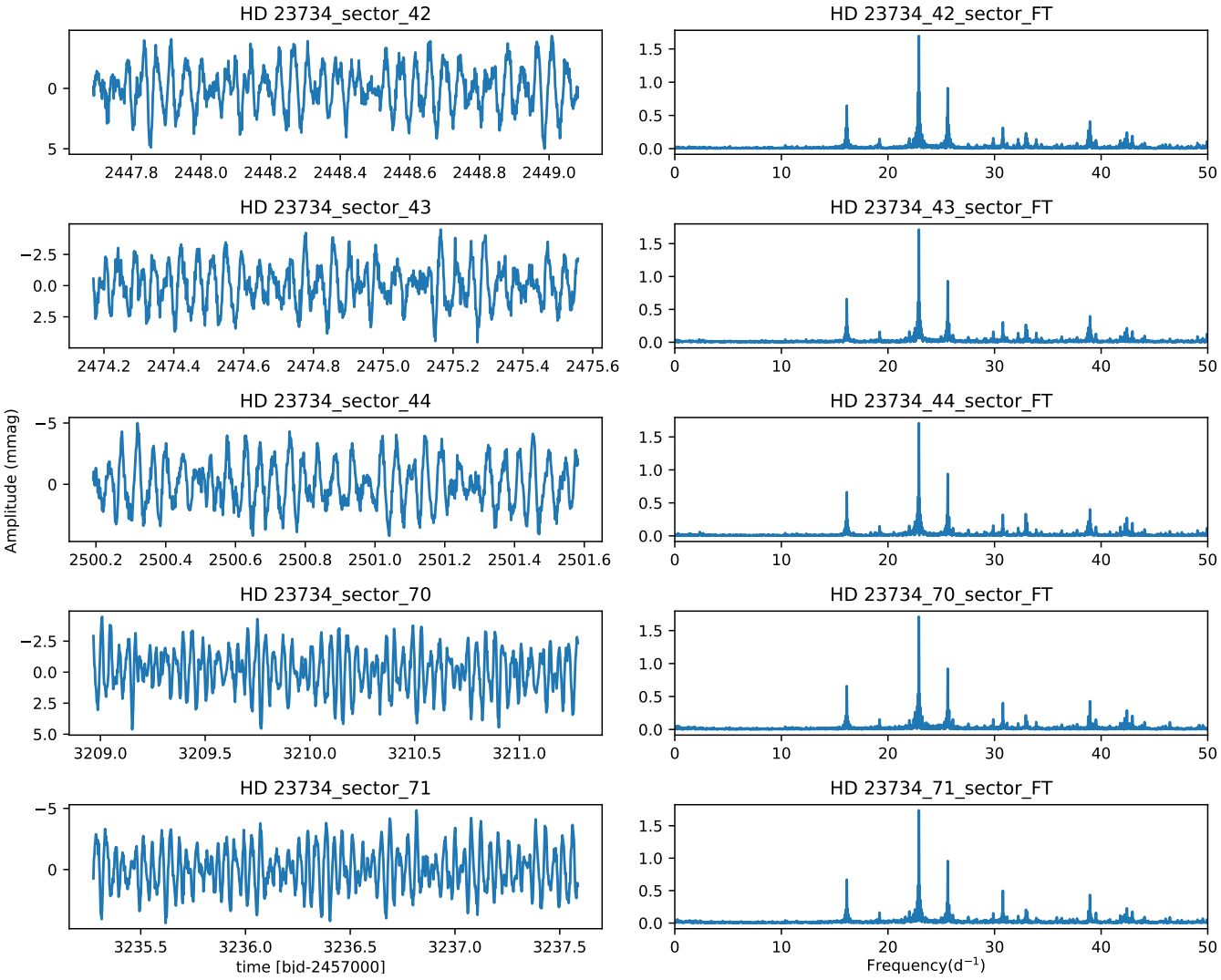

Figure A4. The light curves (left panels) and corresponding frequency spectra (right panels) for HD 23734 obtained with *TESS* in sectors 42, 43, 70 and 71 (from top to bottom row). We plot only up to 50 d^{-1} since we found no significant frequency beyond this point.

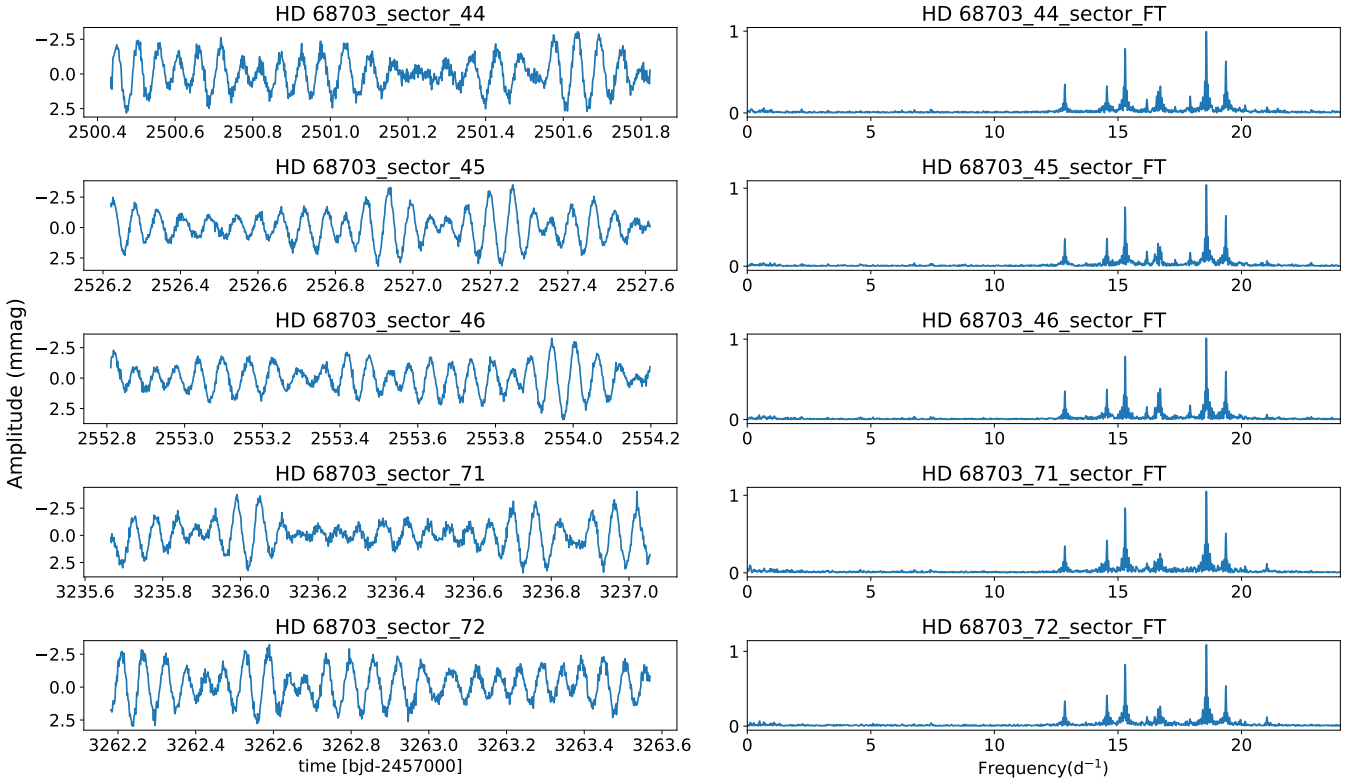

Figure A5. The light curves (left panels) and corresponding frequency spectra (right panels) for HD 68703 obtained with *TESS* in sectors 44, 45, 46, 71, and 72 (from top to bottom row). We plot only up to 24 d^{-1} since we found no significant frequency beyond this point.

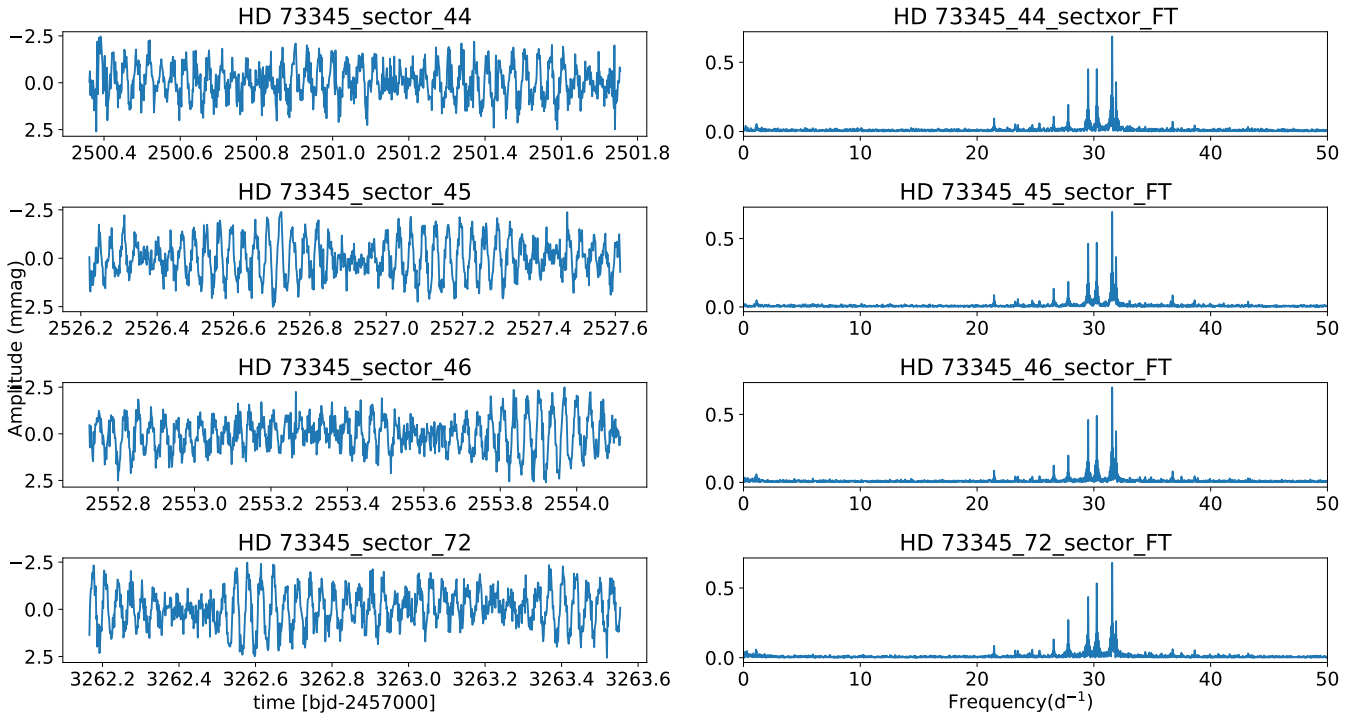

Figure A6. The light curves (left panels) and corresponding frequency spectra (right panels) for HD 73345 obtained with *TESS* in sectors 44, 45, 46, and 72 (from top to bottom row). We plot only up to 50 d^{-1} since we found no significant frequency beyond this point.